Ultrasonic contact pulse transmission for elastic wave velocity and stiffness determination: Influence of specimen geometry and porosity ☆

C. Kohlhauser, C. Hellmich *

Institute for Mechanics of Materials and Structures, Technische Universität Wien, Karlsplatz 13/202, A-1040 Vienna, Austria

ARTICLE INFO

ABSTRACT

Elasticity determination by means of ultrasonic pulse transmission requires experimental realization of non-dispersive, i.e. frequency-independent, wave propagation, be it in form of bulk waves propagating in an (approximately) infinite medium, or of extensional waves propagating through a 1D bar system. While it is conceptually known that wavelengths need to tend towards zero (as compared to the specimen dimensions perpendicular to the pulse propagation direction) in the 3D case, and towards infinity in the 1D case, we here report on a new systematic experimental assessment of the influence of the sample geometry on wave type: tests on solid isotropic aluminum samples reveal that the extensional (or bar) wave propagation mode requires transmission of truly slender samples (required slenderness ratio of 20 or larger for wavelengths equal to the wave travel distance; this minimum slenderness ratio is increasing with increasing travel distance-over-wavelength ratio). After a transition zone with dispersive wave propagation, non-dispersive bulk waves are detected once the slenderness ratio is reduced to 5 or lower (at wavelengths equal to the wave travel distance; this maximum slenderness ratio is increasing with increasing travel distance-over-wavelength ratio). On the other hand, it is conceptually known from continuum mechanics that the wavelength needs to be larger than the investigated material volume or representative volume element (RVE), as to reveal the material's elastic properties, while corresponding quantitative data are rare. As a remedy, we here report on new experiments on transversely isotropic, porous aluminum samples, which reveal that minimum pore dimension-over-wavelength ratios of 1 and 10, respectively, relate to detection of normal and shear stiffnesses, respectively, of the solid material between the pores, while these ratios need to be smaller than 0.01 and 0.1, as to detect the normal and shear stiffnesses of the overall porous materials. The latter can be quantified through various homogenization techniques.

1. Introduction

The design of engineering structures is more and more governed by the development of new construction materials, whose characteristics are not known through long periods of experience, but result from appropriate, comprehensive experimental investigations. Hence, the portfolio of experimental techniques is ever increasing, and the reliability and limitations of such techniques needs to be carefully scrutinized. In the present contribution, we concentrate on a method which is particularly appropriate for elasticity determination, namely the ultrasonic (contact) pulse technique. This technique was originally developed for the detection

of flaws in metals [25,50], and thereafter applied to a wide range of materials, including single crystals [37,50], polycrystalline materials [32,58], polymers [39,28], metals and metal alloys [57,53], composite materials [59,19,48], geomaterials [33,14,40], biological materials such as bone [2] and wood [13,44], as well as biomaterials such as porous titanium and glass-ceramic scaffolds [45].

In the present contribution, we leave aside Rayleigh surface waves, Lamb waves, and guided waves (see e.g. [47,82,76] for detailed explanations), we are also not dealing with plastic waves, shock waves, or viscoelastic waves [14], but our focus lies on elastic waves used in the framework of the so-called transmission through technique. There, an acoustic pulse is introduced at one end of a material sample, and it is measured how long it takes to detect this pulse, after having travelled through the sample, at the opposite end of the sample. The traveling pulse is called wave, and the velocity of the latter is related to the elastic properties of the material. However, there are two limiting cases of such waves: (i) bulk waves, related to propagation of pulses in infinite media and (ii) extensional waves propagating along 'one-dimensional media', i.e. through samples being of very elongated shape,

* Corresponding author. Tel./fax: +43 1 58801 9 20220.
E-mail addresses: Christoph.Kohlhauser@tuwien.ac.at (C. Kohlhauser), Christian.Hellmich@tuwien.ac.at (C. Hellmich).

commonly called bars. While numerous studies [36,62,75,82,30,31] were devoted to the dispersion (i.e. the frequency dependence) of waves in bars fulfilling Pochhammer's boundary conditions [73,15], the frequency-dependent transition of pulse signals, from bulk wave propagation to extensional wave propagation has been quite rarely studied [83,2]. For these limit cases, compact and therefore highly practical mathematical formulae exist. Hence, the question arises under which conditions these limit cases can be experimentally observed in real (i.e. neither infinite 3D, nor perfectly 1D) material samples. It is known from Kolsky [46,47], and considered in subsequent experimental activities [2,45], that the transition from bar to bulk waves starts once the (decreasing) wave length attains the lineal dimension of the cross section of the bar. However, the effect of the bar's slenderness on the type of wave transmitting it, is comparatively unknown, and this is the first main issue to be discussed in the present paper.

Both bulk and extensional waves relate to the long-wavelength-limit, referring to wavelengths being considerably larger than the characteristic length of the material volumes (also called representative volume elements [92]) building up the medium through which the waves travel. If the wavelength attains the size of the material volume, the wave starts to 'feel' the material microstructure, e.g. they may be scattered at inhomogeneities (e.g. inclusions) inside the material volume. The transition from the long-wavelength-limit to waves scattered by microstructural elements has been the topic of various theoretical investigations, be it in the framework of random homogenization theory [60,38,8,78,80,91,90,86] or of periodic homogenization technique [26,49,85,10,11,18,84,65,66,89,27,52,72]. We here do not concentrate so much on this transition, but rather focus on the experimental revelation of two limit cases: the aforementioned long-wavelength-limit (how large needs a wave to be in order to feel the 'homogenized medium' rather than microstructural details?), and also the 'short-wavelength-limit' (how small needs a wave to be to 'feel' the material components themselves, rather than their microstructural interaction?). The short-wavelength-limit was beyond the aforementioned theoretical investigations, relating to the question: how short needs a wave to be in order to find an unscattered path between the microstructural inhomogeneities? Obviously, the answers depend on the type of chosen microstructures. We here choose an extreme case: zero-stiffness, cylindrical pore inclusions.

Accordingly, the paper is organized as follows: after recalling some foundations of plane wave propagation theory (Section 2), we present the ultrasonic measurement system used for the present study (Section 3) and the investigated specimens (Section 4), together with a precision check of our measurement system (Section 5). On this basis, we study the transition from bulk to extensional waves (Section 6), and from the long-wavelength-limit to the short-wavelength-limit (Section 7), both from a dimensional analysis viewpoint. After discussing the experimental results from a micromechanics viewpoint (Section 8), we conclude the paper in Section 9 by giving operational rules for reliable ultrasonic pulse transmission protocols.

2. Wave propagation in 3D and 1D linear elastic solids – theoretical basics

We focus on wave propagation in continua – where the basic property of a continuum solid is that its deformations can be described through representative volume elements (RVEs) 'labeled' on the continuum and staying neighbors during deformation [79]. The characteristic lengths ℓ of such RVEs need to be much smaller than those of the body made up of the RVEs or than the excitation lengths of that body [such as wavelengths λ, see Eq. (7)] – then use of differential calculus is admissible; and the RVE-length ℓ needs to be much larger than the microheterogene-

ities with characterisitic length d within the RVE (e.g. the void diameter in Fig. 1) – then material properties such as stiffness can be introduced. Mathematically, this is expressed by means of the separation-of-scales requirement [92],

$$d \ll \ell \ll \lambda. \tag{1}$$

When considering an infinitely extended 3D medium, the aforementioned stiffness is quantified in terms of the elasticity tensor $\mathbb{C}$, relating (small) strains to stresses. Based on earlier work of Christoffel [16,17], Love [55] was the first to mathematically capture the propagation of elastic waves in infinite three dimensional solids, be they isotropic or anisotropic. In the case of transversely isotropic materials, to which we restrict ourselves in this paper, the independent components of the stiffness tensor are related to velocities of waves traveling in the principal directions of the material, namely in the axial direction (labeled 3), and all directions perpendicular to this axial direction (making up the transverse plane), including directions 1 and 2, being also orthogonal to each other. To fully characterize the aforementioned waves, called bulk waves, also their polarization direction (i.e. the direction of the movement of the material particles or RVEs) needs to be known; and again, we restrict the polarization directions to the principal material directions, and label wave velocities $v_{i,j}$ with two indices, the first one (i) being related to the wave direction, and the second one (j) to the polarization direction. In case of longitudinal waves, the polarization directions coincide with the propagation directions, and corresponding wave velocities are related to normal stiffness tensor components, see e.g. [24,14,44] for details,

$$v_{1,1} = v_{2,2} = \sqrt{\frac{C_{1111}}{\rho}}, \quad v_{3,3} = \sqrt{\frac{C_{3333}}{\rho}}, \tag{2}$$

with ρ as the mass density of the considered material. In case of transverse waves, the polarization direction is perpendicular to the propagation direction, and corresponding wave velocities are related to shear stiffness tensor components, see e.g. [24,14,44] for details,

$$v_{1,2} = v_{2,1} = \sqrt{\frac{C_{1212}}{\rho}}, \quad v_{1,3} = v_{3,1} = v_{2,3} = v_{3,2} = \sqrt{\frac{C_{1313}}{\rho}}. \tag{3}$$

In case of isotropy, wave propagation velocities are independent of the propagation direction, and in all directions, the wave velocities follow from specification of (2) and (3) for $C_{3333} = C_{1111}$ and $C_{1313} = C_{1212}$ so that we have

$$v_L = \sqrt{\frac{C_{1111}}{\rho}} \quad \text{and} \quad v_T = \sqrt{\frac{C_{1212}}{\rho}}, \tag{4}$$

with v_L and v_T as the velocities of longitudinal and transverse (or shear) waves in isotropic media. Since isotropic solids are completely described by two elastic constant, e.g. C_{1111} and C_{1212} (the shear modulus G is equal to the shear stiffness component, i.e. $G = C_{1212}$), the two velocities v_L and v_T can also be used to determine two engineering elastic constants, e.g. Young's modulus and Poisson's ratio, in the form

$$E = \rho \frac{v_T^2 (3v_L^2 - 4v_T^2)}{v_L^2 - v_T^2} \quad \text{and} \quad v = \frac{v_L^2/2 - v_T^2}{v_L^2 - v_T^2}. \tag{5}$$

When considering 1D media, i.e. bars characterized by a one-dimensional state of normal stress, there is only one (extensional or bar) wave propagating through the considered bar, with its wave velocity being related to the Young's modulus E of the material, see [46] for details,

$$v_E = \sqrt{\frac{E}{\rho}}. \tag{6}$$
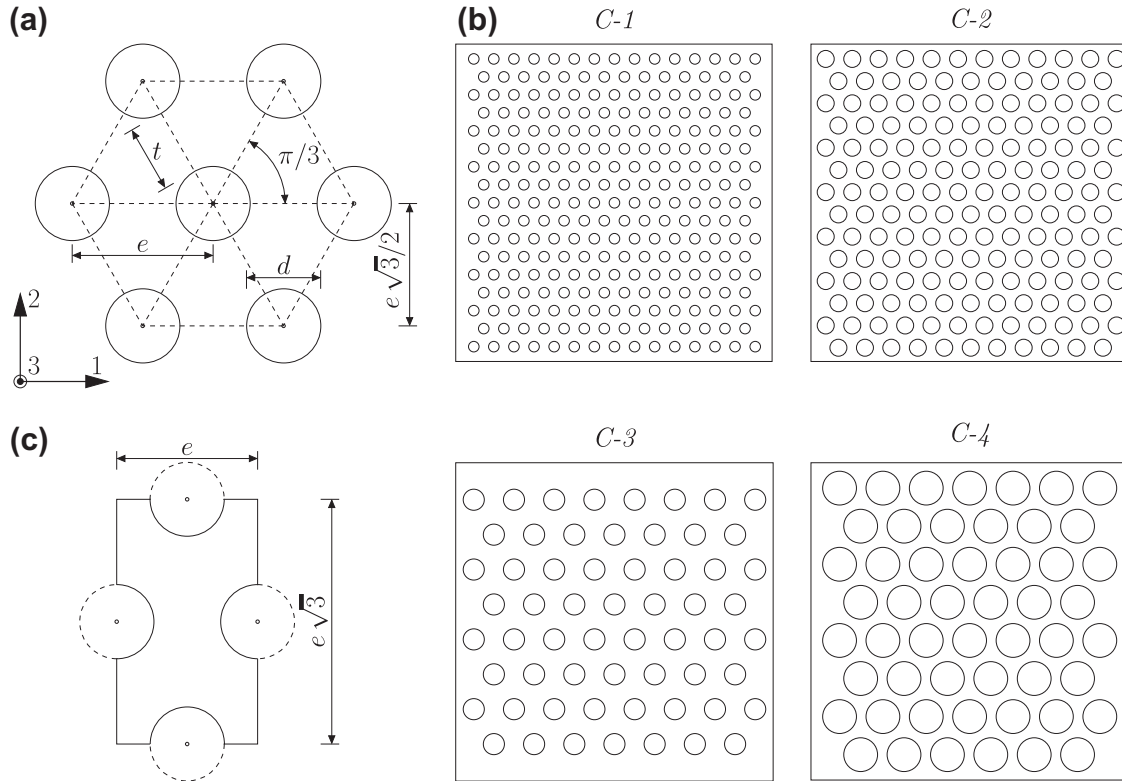
Fig. 1. Specimens for investigation of microstructure (porosity) on wave propagation velocity: (a) Porous cylinders in hexagonal arrangement (and definition of principle material directions), (b) arrangements of voids in specimens of *set C*, and (c) unit cell.

The wavelengths λ of the aforementioned longitudinal, shear, and extensional waves depend on their (phase) velocity v_p as well as on the frequency f of the pulse traveling through the tested solid [68,14]

$$\lambda = \frac{v_p}{f}. \tag{7}$$

3. Ultrasonic measurement system

3.1. Equipment and set-up

The employed equipment consists of an ultrasonic pulser and a signal receiver built into a single unit (PR 5077, Panametrics Inc., Waltham, MA, USA; see Fig. 2a); a digital oscilloscope (WaveRunner 62Xi, Lecroy Corporation, Chestnut Ridge, NY, USA; see Fig. 2a); 17 pairs of ultrasonic, single-element, untuned contact transducers for longitudinal and transverse pulses (Panametrics Inc., Waltham, MA, USA; see Table 1), with pulse frequencies ranging from 0.1 to 20 MHz and corresponding pulse widths ranging from 10 to 0.05 μs; an ultrasonic signal preamplifier (5676, Panametrics Inc., Waltham, MA, USA); a coupling medium (honey); and an auxiliary testing device (see Fig. 2a); for more details of the equipment, we refer to [43].

We here use the transmission-through technique, where two transducers are used, one sending a signal into the specimen and one receiving the sent signal on the opposite side of the specimen (see Fig. 2a).

The time of flight of the signal through the specimen, t_f, provides, together with the travel distance through the specimen, h, the signal velocity,

$$v = \frac{h}{t_f}. \tag{8}$$

If the wave is not scattered at material inhomogeneities being of the same order of magnitude as the wavelength, i.e. if the wavelength is either much larger than these inhomogeneities ('long-wave-limit'), or so small that it detects a continuous straight material path between these inhomogeneities ('short-wave-limit'), then the aforementioned signal velocity is identical to the phase velocity v_i of the longitudinal ($i = L$) or transverse ($i = T$) wave, being related to the stiffness of the sonified material through Eqs. (2) and (3), respectively. Thereby, t_f is determined by the difference of the total time of flight measured between the transducers, t_{tot}, and the wave transit time without the specimen, called system and transducer delay time t_d (see Table 1, columns five and nine). t_d includes the time delay caused by the transducers, by the coupling medium, by additional delay lines, and by the measurement system itself. The benchmark for the time of flight measurements is a reference signal sent by the ultrasonic pulser–receiver, on which the trigger of the oscilloscope is set. Since we are interested in the first arrival of the ultrasonic wave (even in case the pulse is strongly attenuated and consequently, the wave form is changed, i.e. broadened), we use the first apparent deviation of the received signal from constancy with time (i.e. the time instant when the signal rises beyond noise level) as the arrival time of the ultrasonic wave; as it was done by Nicholson and Strelitzki [69]. Transversal wave propagation is usually accompanied by a precursor longitudinal wave (see e.g. [70,47,71,74]). In cases where the precursor longitudinal wave interferes with the first arrival of the transverse wave, the wave trough preceding the main transverse wave crest is used to determine the wave arrival time.

The time readings on the oscilloscope are performed manually. The deviation of the received pulse from the time constancy axis develops smoothly. Therefore, the signal amplitude and frequency (of both pulser–receiver and transducer), as well as the amplitude and time range chosen for display of the pulse on the oscilloscope,
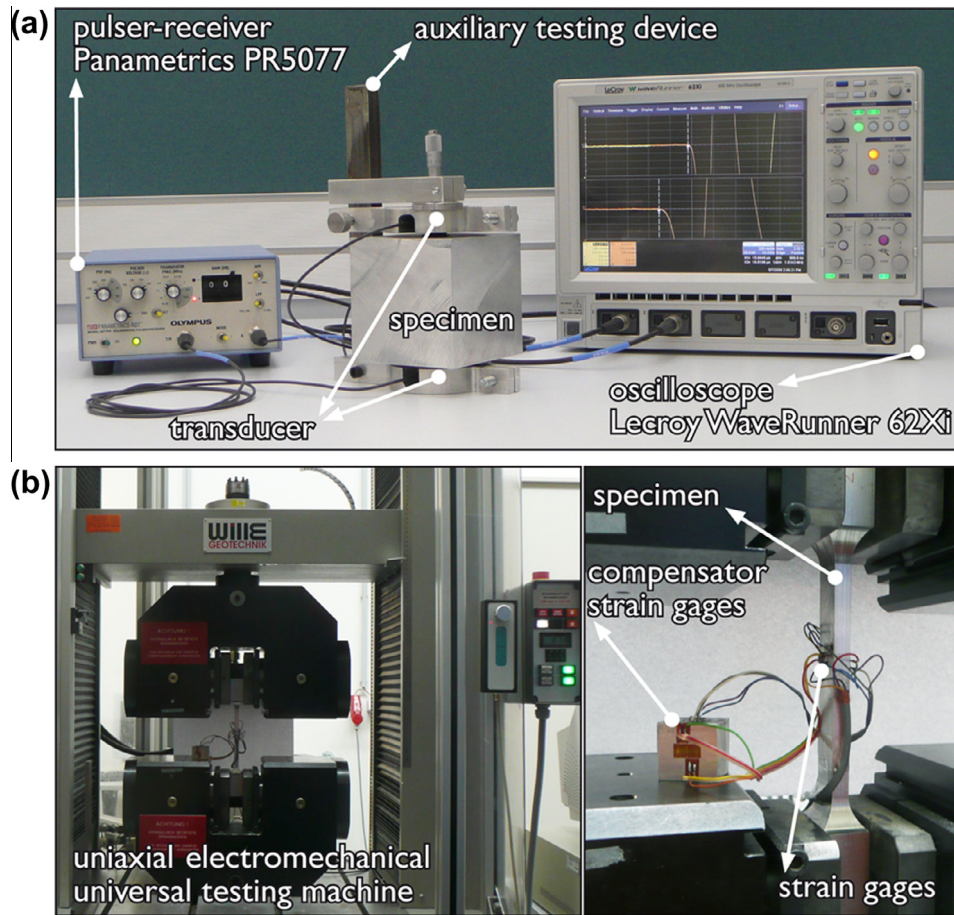
Fig. 2. Determination of stiffness constants of aluminum alloy 5083. (a) Ultrasonic velocity measurements. (b) Quasi-static mechanical tests.

Table 1
Ultrasonic longitudinal and transverse transducers (frequency f, aluminum-related wavelength λ_i, element diameter d_e, system and transducer delay time t_d).

f (MHz)	Longitudinal				Transversal			
	λ_L (mm)	Label (–)	d_e (mm)	t_d (µs)	λ_T (mm)	Label (–)	d_e (mm)	t_d (µs)
0.05	127	X1021	32	3.988	–	–	–	–
0.1	64	V1011	38	3.667	32	V1548	25	0.339
0.25	25	V1012	38	3.355	13	V150-RB	25	0.351
0.5	13	V101-RB	25	2.464	6.4	V151-RB	25	0.390
1.0	6.4	C602-RB	25	2.828	3.2	V152-RB	25	0.320
2.25	2.8	C604-RB	25	2.555	1.4	V154-RM	13	0.211
5.0	1.3	C109-RM	13	2.426	0.6	V155-RM	13	0.147
10	0.6	V112-RM	6	2.343	0.3	V221-BA-RM	6	6.939
20	0.3	V116-RM	3	2.346	0.16	V222-BA-RM	6	6.928

influence the time readings of signal arrival. In order to obtain comparable results, measurements were performed, as a rule, at fixed pulse voltage (100 V) and gain settings (30 dB) on the pulser–receiver, which was set to 100 Hz pulse repetition rate. Only in case a higher pulse energy was necessary to penetrate the specimen with a signal amplitude that allowed for precise time readings, a gain of 40 dB was used, together with a higher pulse voltage, namely 400 V for transducers with frequencies lower than 5 MHz, and 300 V for all other transducers (in order to protect the smaller piezoelectric crystals of the latter from overheating and depoling). In order to smoothen the wave signal at pulse frequencies below 5 MHz, the low pass filter was used, which inhibits frequencies higher than 10 MHz.

Also the display settings on the oscilloscope were fixed, namely at a sample rate of 10 GS/s, at a time range of 5 µs, and at an amplitude range of ±0.4 V. The bandwidth was limited to 20 MHz for transducers below 5 MHz, and to 200 MHz for higher frequency transducers, as to minimize signal noise. For the arrival time reading the first arrival part of the pulse was displayed in an additional zoom window, covering 1 µs and ±0.4 V in time and amplitude dimensions, respectively. The accuracy of cursor positioning was 0.1 ns, but reliable measurements were only possible up to an accuracy of 10 ns = 0.01 µs.

The exact identification of the signal arrival time is the major source of measurement inaccuracies. Especially for small thicknesses of the specimens and corresponding short times of flight and/or low transducer frequencies, this error may be essential. In order to minimize this error (as well as other sources of inaccuracies), delay lines have been used since the beginning of ultrasonic research [1]. Such delay lines may fulfill two purposes: (i) the near

field of the transducer, located directly adjacent to the wear plate and characterized by an oscillating amplitude, is relocated out of the investigated specimen [88] and (ii) the received pulse (arrival signal) is relocated out of the time range of receiver disturbances stemming from the electrical ignition of the pulser. The latter purpose is relevant here, since our present focus is on arrival times rather than on amplitude measurements. We used as delay lines cylinders made of aluminum alloy 5083 with diameters 1.5 mm larger than the diameter of the transducers ($\approx d_e$ in Table 1), as to leave room for a notch that prevents the delay line from slipping between the transducer and the specimen. The heights of the delay lines were 15 mm and 20 mm, respectively, referring to a time delay of 2.35 μs and 3.14 μs, respectively. They were coupled to the sending transducers with honey. The longer time delay was used for the longitudinal transducers with the three lowest frequencies (f = 0.05, 0.1, 0.25 MHz), while the shorter time delay was used for the rest of the longitudinal transducers. Implementation of the delay lines led to higher accuracy over all frequencies when sending longitudinal waves through thin specimens. Such a positive effect was not observed with transverse waves. On the contrary, delay lines even impaired the measurement results of low frequency transverse waves, due to the more complicated experimental setup (including a third coupling layer), which makes the discrimination of the correct wave crest more difficult. Thus, with transverse transducers no delay lines were used, except for the two transverse transducers with the highest frequencies, which have a built-in silica delay line (delay time ≈ 6.8 μs; see Table 1).

In order to minimize errors in time of flight measurements, we standardly employed two transducers of identical architecture and center frequency for the pulse-transmission measurements. As exception to that rule, the longitudinal and transverse transducers with center frequencies of 20 MHz were used in combination with the equivalent 10 MHz-transducers as receivers; the 0.05 MHz- and 0.1 MHz-longitudinal transducers were used in combination with a 0.1 MHz-longitudinal transducer (X1020, d_e = 16 mm) as receiver; and the 0.25 MHz-longitudinal transducer was used in combination with the 0.5 MHz-longitudinal transducer as receiver (see Table 1). These exceptions were allowed since using a receiving transducer with a center frequency differing from that of the sending transducer did not remarkably change the test results on one and the same specimen.

When combining ultrasonic longitudinal and transverse velocity measurements, e.g. for the computation of engineering elastic constants (see Eq. (5)), only values related to comparable wavelengths should be used, referring to the same scale of mechanical investigation (see Eq. (1)). The transverse wave velocity is approximately half of the longitudinal one, over most (isotropic) materials. From Eq. (7) it follows that, in order to achieve equal wavelengths $\lambda_L = \lambda_T$, a longitudinal frequency transducer should be combined with a transverse transducer exhibiting half the frequency of the longitudinal one, i.e. $f_T = f_L/2$ (see also Table 1, columns two and six).

Other sources of measurement errors include the flatness of the specimen surfaces where the transducers are applied, if these surfaces are not strictly parallel; and the character of the coupling layer. It is important to realize an evenly distributed coupling layer of constant thickness, without (air) inclusions. Measurements were performed near room temperature (i.e. ≈ 300 K, ≈ 25 °C). According to Ledbetter [51] a 10-K temperature change alters (copper) ultrasonic velocities by only 0.05%, implying that the expected temperature variations [4] in laboratories do not significantly affect corresponding results.

3.2. Error propagation

All spatial dimensions of specimens were determined from the average of five measurements with a micrometer gauge

characterized by a precision of ±10 μm. Masses were measured on a digital balance, with a precision of ±1 mg. Then the apparent density ρ_{app} was determined, as the ratio of mass m and volume V

$$\rho_{app} = \frac{m}{V}, \tag{9}$$

whereby our cuboidal specimens (see Section 4 for more details) are characterized by height h and quadratic cross-section with edge length a, so that

$$V = ha^2. \tag{10}$$

In the sequel, we discuss how measurement errors in fundamental quantities, such as length (h, a), mass (m), and time of flight (t_f) affect errors in the following derived quantities [77]: volume V (Eq. (10)), density ρ_{app} (Eq. (9)), velocity v_i (Eq. (8)), and stiffnesses C_{ijkl} or E (Eqs. (2), (3), (4), (6)). Therefore, we recall the law of error propagation [64]

$$s_y^2 \approx \sum_i \left(\frac{\partial \mathscr{F}}{\partial x_i} s_i \right)^2 + 2 \sum_{i<j} \frac{\partial \mathscr{F}}{\partial x_i} \frac{\partial \mathscr{F}}{\partial x_j} s_{ij} \quad i,j = 1, 2, \ldots, n, \tag{11}$$

where s_y is the standard deviation of a random variable y, which is generated by evaluating a deterministic function $\mathscr{F}$ of n random variables x_i characterized by variances s_i^2 and covariances s_{ij}. Depending on the investigated quantity, $\mathscr{F}$ is chosen as V, ρ_{app}, v_i, C_{ijkl}, or E (according to Eqs. (10), (9), (8), (2)–(4), (6)), and the variables x_i are chosen as h, a, m, V, t_f, ρ_{app}, and/or v_i. If the variables x_i are uncorrelated, the last term in (11) vanishes. Approximation (11) is valid for small random alterations of the variables x_i, and implies that all errors are random, i.e. systematic errors are assumed to be zero. Thus, strictly speaking, we give precisions (reproducibility) rather than accuracies of measurements. The standard deviations s_i [also referred to as uncertainties or as errors [64]] give access to the relative standard deviations (relative errors) δ_i, via

$$\delta_i = \frac{s_i}{x_i}. \tag{12}$$

Using this definition and the definition of the correlation coefficient $\delta_{ij} = s_{ij}/(s_i s_j)$, specifications of $\mathscr{F}$ according to (10), (9), (8), and (2) (or (3), (4), (6)) yields

$$\delta_V = \sqrt{\delta_h^2 + 2\delta_a^2}, \tag{13}$$

$$\delta_\rho = \sqrt{\delta_m^2 + \delta_V^2 - 2\delta_m \delta_V \delta_{mV}}, \tag{14}$$

$$\delta_v = \sqrt{\delta_h^2 + \delta_t^2 - 2\delta_h \delta_t \delta_{ht}}, \tag{15}$$

$$\delta_C = \sqrt{4\delta_v^2 + \delta_\rho^2 + 4\delta_\rho \delta_v \delta_{\rho v}}, \tag{16}$$

whereby δ_h is the relative error in h, and so forth. Based on (absolute) errors of $s_h = s_a = 0.01$ mm (precision of the micrometer gauge), Eqs. (12) and (13) give access to the relative errors in h, a, and V, see columns four to six in Table 2. Considering additionally $s_m = 0.001$ g (precision of the digital balance) and $\delta_{mV} = 1.00$ (as obtained from a statistical analysis of the measurements on all dense aluminum samples of Section 4, see Table 3, column three), Eqs. (12) and (14) give access to the relative errors in m and ρ, see columns seven and eight of Table 2. The latter value was checked by computing δ_ρ directly from the measurements on all plate-type, cubic, and bar-type dense specimens, yielding 0.187%, which underlines the relevance of error propagation law (11) for our purposes (see Table 2, column eight, rows three to five).

The uncertainties in time of flight, s_t, are (conservatively) estimated, for each frequency, from the range of time instants in which the first deviation of the signal from the time constancy axis can be discerned (see Table 3, column two). This value for s_t gives access to the corresponding relative errors according to Eq. (12), $\delta_t = s_t/t$,

Table 2
Geometrical dimensions of specimens, with corresponding relative errors δ_h, δ_a, δ_v, δ_m, and δ_ρ, and times of flight t_f related to longitudinal waves.

Geometry	h (mm)	a (mm)	δ_h (%)	δ_a (%)	δ_V (%)	δ_m (%)	δ_ρ (%)	t_f (μs)
Thin plate	0.5	30	2.00	0.03	2.001	0.084	1.917	0.078
Plate	5	30	0.20	0.03	0.205	0.008	0.197	0.785
Cube	30	30	0.03	0.03	0.058	0.001	0.056	4.708
Bar	30	1	0.03	1.00	1.415	1.255	0.160	4.708
Long bar	100	1	0.01	1.00	1.414	0.376	1.038	15.69

Table 3
Standard deviations in the time of flight, s_t, as well as correlation coefficients δ_{mV}, δ_{ht}, and $\delta_{\rho v}$, given for different frequencies.

f (MHz)	s_t (μs)	δ_{mV} (−)	δ_{ht} (−)	$\delta_{\rho v}$ (−)
0.05, 0.1	0.10	1.000	0.995	0.249
0.25, 0.5, 1.0	0.05	1.000	0.996	0.029
2.25, 5	0.02	1.000	0.997	0.127
10, 20	0.01	1.000	0.998	0.122

based on the times of flight of longitudinal (bulk) waves, observed at different geometries (see Table 4, column two). Because of $v_T \approx v_L/2$, transverse waves exhibit double times of flight and half relative errors δ_t, when compared to those of longitudinal waves. Relative errors of velocity δ_v are determined via (15), with δ_h according to column four in Table 2, with δ_t according to column two in Table 4, and with the correlation coefficient of δ_{ht} according to column four in Table 3. Thereby, δ_{ht} is obtained from length and time of flight measurements on all (dense) specimens belonging to one of the frequency groups given in Table 3. Significant relative errors δ_v occur for low frequency measurements in thin specimens (see Table 4). The relative velocity errors for high frequencies are in accordance with Ledbetter [51], who gives $\delta_v < 0.1\%$ for box-shaped copper specimens ($h = 19$ mm, $t \approx 4$ μs, $f = 3$–10 MHz). The relative error in stiffnesses, δ_C, (see column four in Table 4) is estimated through Eq. (16), with δ_ρ according to column eight in Table 2, δ_v according to column three in Table 4, and $\delta_{\rho v}$ according to column

Table 4
Relative errors δ_i in time of flight, velocity and stiffnesses, given for different specimen geometries and different frequencies.

f (MHz)	δ_t (%)	δ_v (%)	δ_C (%)
Thin plate			
0.05, 0.1	127	126	251
0.25, 0.5, 1.0	64	62	124
2.25, 5	25	24	47
10, 20	13	11	22
Plate			
0.05, 0.1	12.7	12.5	25.1
0.25, 0.5, 1.0	6.4	6.2	12.4
2.25, 5	2.5	2.3	4.7
10, 20	1.3	1.1	2.2
Cube			
0.05, 0.1	2.12	2.09	4.20
0.25, 0.5, 1.0	1.06	1.03	2.06
2.25, 5	0.42	0.39	0.79
10, 20	0.21	0.18	0.37
Bar			
0.05, 0.1	2.12	2.09	4.22
0.25, 0.5, 1.0	1.06	1.03	2.07
2.25, 5	0.42	0.39	0.82
10, 20	0.21	0.18	0.41
Long bar			
0.05, 0.1	0.64	0.63	1.82
0.25, 0.5, 1.0	0.32	0.31	1.22
2.25, 5	0.13	0.12	1.09
10, 20	0.06	0.05	1.06

five in Table 3. Thereby, $\delta_{\rho v}$ is obtained from density and velocity measurements on all (dense) specimens belonging to one of the frequency groups of Table 3. In case $\delta_\rho \ll \delta_v$ (e.g. at lower frequencies, i.e. higher δ_v), or if ρ is a precisely known quantity, Eq. (16) reduces to

$$\delta_C = 2\delta_v, \tag{17}$$

i.e. the relative error doubles when deriving stiffness tensor components from measured ultrasonic velocities. This was approximately observed when computing relative errors δ_v and δ_C directly from (bulk) velocity measurements on dense specimens *A-5* to *A-12* (see following section) and from the density measurements discussed below Eq. (16). We re-iterate that the errors given in Table 4 are due to measurement uncertainties and that they do not include other error sources, such as uneven surfaces. From the results in Table 4 it is evident that very high errors are only to be expected if very thin samples, characterized by short times of flight, are investigated at low frequencies. Conclusively, when considering all sources for inaccuracies, the ultrasonic contact pulse-transmission technique is in general satisfactorily exact.

4. Specimens for ultrasonic tests

All specimens were made of commercial aluminum alloy EN AW-5083-H111, produced according to the European standards EN-485-1 [21] and EN-485-2 [22], a material that is insensitive to temperature changes in the room temperature regime [87]. The specimens are subdivided into five sets. *Set A1*, *A2*, *B*, and *R* are used to investigate the effect of specimen geometry and size on ultrasonic wave propagation (see Table 5), and *set C* is used to investigate the effect of specimen microstructure (see Table 6). All specimens are box-shaped with characteristic cross-sectional dimension a (edge length of the two specimen surfaces having the shape of a square) and height h; except for specimens *R-2* and *R-3*, which are cylindrically shaped; there, a equals the diameter.

In addition, an aluminum cube with an edge length of $a = h = 100$ mm (cut from a 100 mm thick plate) was used to obtain reference bulk wave velocities (even for lower frequencies, as will be verified in Section 6).

The 12 specimens of *set A1* have a constant height $h = 30$ mm, but varying characteristic cross-sectional dimensions a ranging from 1 to 100 mm, therefore covering shapes ranging from bars, via cubes, to (thick) plates. *Set A2* consists of six specimens with a constant cross-sectional dimension of $a = 3$ mm, but with varying heights h from 30 to 110 mm, i.e. these specimens are bars of different slenderness. *Set B* consists of 12 specimens with constant $a = 30$ mm and h varying from 0.5 to 30 mm, i.e. covering shapes ranging from (thin) plates to cubes. *Set R* consists of a bar with the lowest ratio a/h, namely 0.01, and of two cylindrical specimens. *Set C* consists of four box-type aluminum specimens with cylindrical voids of different diameters d, in a hexagonal arrangement with different distances e between the cylinder axes, resulting in different porosities (see Fig. 1a and b and columns four and five in Table 6). Hexagonal symmetry is characterized by a 6-fold axis, i.e. a rotation by $\pi/3$ about axis 3 (longitudinal cylinder direction,

Table 5
Aluminum specimen *set A1*, *A2*, *B*, and *R* – influence of geometry on wave propagation (dimensions in (mm)).

Set A1			Set A2			Set B		
#	a	h	#	a	h	#	a	h
1	1	30	1	3	30	1	30	0.5
2	2	30	2	3	40	2	30	1
3	3	30	3	3	60	3	30	2
4	5	30	4	3	70	4	30	3
5	10	30	5	3	90	5	30	4
6	15	30	6	3	110	6	30	5
7	20	30				7	30	7.3
8	30	30				8	30	10
9	40	30		Set R		9	30	15
10	50	30	1	1	100	10	30	20
11	75	30	2	9	14	11	30	25
12	100	30	3	18	4	12	30	30
A2-1 = A1-3						B-12 = A1-8		

Table 6
Aluminum specimen *set C* – influence of microstructure on wave propagation (see Fig. 1 for definition of *d* and *e*).

#	ρ (g/cm^3)	φ (%)	d (mm)	e (mm)	a (mm)	h (mm)
1	2.07	21.9	1.0	2.03	30	20
2	1.79	32.7	1.5	2.50	30	30
3	2.05	22.8	2.0	3.99	30	30
4	1.36	48.7	3.2	4.37	30	30

see Fig. 1a) does not change the elastic stiffness, which – in turn – implies invariance against rotation by *any* angle [33]. Materials with one axis of complete rotational invariance are termed transversely isotropic. Four different drill bit diameters, namely $d = 1$, 1.5, 2, 3.2 mm were used to produce four specimens (termed *C-1*, *C-2*, *C-3*, and *C-4*), with 247, 161, 60, and 52 boreholes, respectively (see Fig. 1b), and with three different porosities (specimens *C-1* and *C-3* have approximately the same porosities, see column three in Table 6). Specimens *C-2*, *C-3*, and *C-4* are cubes with an edge length of $a = h = 30$ mm. The height of specimen *C-1* was reduced to $h = 20$ mm, in order to reduce problems in the deep drilling regime (characterized by drilling depth larger than 10 times the drill bit diameter, i.e. 10 mm in case of the 1 mm boreholes). The wall thickness $t = e - d$ (see Fig. 1a), i.e. the thinnest part of solid matrix between the boreholes, is approximately 0.9 mm in specimens *C-1*, *C-2* and *C-4*, and 1.8 mm in specimen *C-3* (see Fig. 1b).

The geometrical properties of *set C* in Table 6 are determined by measuring the mass m and volume V for each specimen, and by computing the apparent density ρ_{app} according to (9). Knowing the apparent density ρ_{app} and the density of the solid, $\rho_s = 2.656$ g/cm^3 (see Table 7), the porosity φ (–) is given by:

$$\varphi = \frac{\rho_s - \rho_{app}}{\rho_s}. \tag{18}$$

For an exactly (infinite) hexagonal arrangement of cylindrical voids, the porosity is proportional to the square of the ratio of the diameter of the voids d to their distance e,

$$\varphi = \frac{\pi}{2\sqrt{3}} \frac{d^2}{e^2}. \tag{19}$$

Knowing φ from measurements of the actual specimen (18) and d from the diameter of the drill bit, an average value for the actual size of e follows from (19) assuming an exact (infinite) hexagonal structure. The deviation of this actual (average) borehole distance e from its theoretical analogon related to an exact (infinite) hexagonal structure according to Fig. 1, amounts to about 5% for all considered specimens. This is due to the inaccuracies in the borehole

pattern, to the deviation of the borehole from the longitudinal direction, and to lack of boreholes in the borderarea (the realization of which was beyond the scope of this work, and would also have complicated the coupling of transducer and specimen). The actual porosity (see column three in Table 6) deviates from the infinite hexagonal structure porosity by around 10% for each specimen, so that our specimens can be regarded as decent approximation of quasi-infinite porous hexagonal patterns.

5. Bulk wave propagation: precision check

In order to check the precision of our ultrasonic measurement system, we compare bulk wave velocities measured on a cube of aluminum alloy 5083 with $a = h = 100$ mm (Fig. 2a), with wave velocities found in the literature, and with wave velocities back-calculated from quasi-static tests performed in our laboratory (Fig. 2b). Corresponding results are collected into Table 7.

In our ultrasonic tests (see column two of Table 7), the wave velocity was measured with all nine longitudinal and eight transverse contact transducers, both with and without delay line. Each of these velocity values was determined from an average of at least three (actually three or four) independent time of flight measurements, i.e. a total of more than 100 measurements were available. The longitudinal and transverse bulk wave velocities were determined from 18 and 16 average results, respectively. The extensional velocity and the elastic constants were determined from the 14 average results, each one corresponding to equal longitudinal and transverse wavelengths (see Table 7, column two).

When taking the average of eight values from four different literature sources [87,67,6,61], we observe that the off-diagonal component C_{1122} shows by far the highest standard deviation of all, but that the average stiffness values agree very well with our own measurements (Table 7, columns three and two).

The mass density $\rho_s = 2.656$ g/cm^3 was determined on an aluminum cube with an edge length of 100 mm, according to Eq. (9) with $\rho_s = \rho_{app}$; this measurement was repeated twice.

Quasi-static load-controlled tensile tests were performed on a uniaxial electromechanical universal testing machine (LFM 150, Wille Geotechnik, Germany, see Fig. 2b). Three dog bone-shaped specimens with constant rectangular cross-section of 30×10 mm over the measurement range of 150 mm (gradually broadened, over 10 mm, up to a cross-section of 50×10 mm in the clamping area) were made from the same aluminum alloy plate as was used for the production of the specimens for ultrasonic tests. The load was applied up to a stress σ_j of 75 MPa, with a stress rate of 0.17 MPa/s. The axial normal strains ε_j (those in direction of tensile force) and the lateral normal strains ε_i (those in direction perpendicular to tensile force) were measured by means of two separate Wheatstone bridge circuits of strain gauges (3/350XY13, Hottinger Baldwin Messtechnik GmbH, Germany) for compensation of any bending moment influences, yielding Young's modulus and Poisson's ratio of an isotropic material, according to

$$E_{qs} = \frac{\sigma_j}{\varepsilon_j} \quad \text{and} \quad v_{qs} = -\frac{\varepsilon_i}{\varepsilon_j}, \tag{20}$$

respectively. The average of the results from the loading and the unloading path, respectively, was taken for each test (the corresponding differences amounted to less than 0.5%), and each of the three specimens was tested twice (the differences resulting from test repetition amounted to less than 0.5‰). For each set of E_{qs} and v_{qs}, the other elastic constants and ultrasonic wave velocities were determined (average values and standard deviations in percent of average given in Table 7, column four).

The results from both measurement methods, quasi-static and ultrasonic, show good agreement with average literature values

Table 7
Elastic stiffness and ultrasonic bulk velocities of aluminum alloy 5083, from literature Weston et al. [87], Naimon et al. [67], Benck and Filbey [6], and Matweb [61] (lit), and from our own quasi-static (qs) and ultrasonic (us) tests (average values ± standard deviation in percent of average; bold values measured or from literature, remaining derived from these via Eqs. (4)–(6)).

Quantity (unit)	Ultrasonic (own experiment)	Ultrasonic (literature)	Quasi-static (own experiment)	Deviation us	
				Lit	Qs
n (–)	14	8	3	–	–
ρ (g/cm^3 ± %)	**2.656**	**2.663 ± 0.1**	**2.656**	0.3	–
v_L (km/s ± %)	**6.372 ± 0.2**	6.349 ± 2.6	6.301 ± 1.5	−0.4	−1.1
v_T (km/s ± %)	**3.205 ± 0.7**	3.170 ± 0.6	3.263 ± 1.4	−1.1	1.8
v_E (km/s ± %)	5.229 ± 0.6	5.176 ± 0.3	5.295 ± 1.4	−1.0	1.3
C_{1111} (GPa ± %)	107.86 ± 0.3	107.47 ± 5.2	105.49 ± 3.0	−0.4	−2.2
C_{1212} (GPa ± %)	27.29 ± 1.4	**26.78 ± 1.2**	28.29 ± 2.9	−1.9	3.6
C_{1122} (GPa ± %)	53.36 ± 1.8	53.91 ± 11.2	48.92 ± 3.2	1.0	−8.3
E (GPa ± %)	72.63 ± 1.2	**71.40 ± 0.7**	**74.49 ± 2.9**	−1.7	2.6
v (– ± %)	0.331 ± 1.1	0.333 ± 3.8	**0.317 ± 0.3**	0.8	−4.2
C_{1111}/E (– ± %)	1.486 ± 1.3	1.505 ± 5.1	1.416 ± 0.3	1.3	−4.7

(compare Table 7, columns two to four). The ultrasonic stiffness measurements differ by at most 2% from literature values (see Table 7, column five). Ultrasonic wave velocities agree even better, with a deviation of only 1%. Excellent agreement is also found between the two different experimental setups, i.e. quasi-static and ultrasonic measurements (see Table 7, column six). Again the off-diagonal component exhibits the highest discrepancy between test methods (8%), for all other values, the difference is at most 4%.

6. Sample-specific wave propagation – bulk waves and extensional waves

According to the theory of elastic waves in infinite isotropic solids (built up by RVEs which are far smaller than the wavelengths λ), the longitudinal wave velocity is given through [55,46,41,3,14], see also (4)$_1$,

$$v_L = \sqrt{\frac{C_{1111}}{\rho}},\tag{21}$$

with C_{1111} as the normal stiffness component of the material, and ρ as its mass density. For bounded solids, such as the box-type samples with square-shaped cross sections investigated in the present study, v_L additionally depends on sample height h, edge length a, and (longitudinal) wavelength λ_L,

$$v_{L,exp} = F(C_{1111}, \rho, a, h, \lambda_L).\tag{22}$$

Thanks to the dimensional independence of C_{1111}, ρ, and h, dimensional analysis [12,5] allows for reducing the function F of four dimensional arguments (see (22)) to a (dimensionless) function of only two dimensionless arguments, reading as:

$$\frac{v_{L,exp}}{\sqrt{C_{1111}/\rho}} = \mathscr{F}\left(\frac{a}{h}, \frac{h}{\lambda_L}\right),\tag{23}$$

which, according to Eq. (21), is equivalent to

$$\frac{v_{L,exp}}{v_L} = \mathscr{F}\left(\frac{a}{h}, \frac{h}{\lambda_L}\right).\tag{24}$$

In principal, Eqs. (23) and (24) describe classes of similar problems defined through the same dimensionless quantities, being not restricted to a specific material, but valid for all materials with RVEs significantly smaller than the encountered wavelengths [compare Eq. (1)]. We are left with determination of $\mathscr{F}$ from our test series A1, A2, B, and R (performed on a specific material, aluminum alloy 5083):

Tests on sample *set A1* (solid aluminum boxes characterized by constant heights of 30 mm, and by square-shaped cross sections with edge lengths varying from 1 mm to 100 mm, passing all the shapes from plate-like, via cubic, to bar-like, see Table 5) reveal that longitudinal wave velocities increase with increasing cross section, unless they reach a constant value, which coincides with the bulk velocity of aluminum, $v_L = \sqrt{C_{1111}/\rho}$, see Fig. 3a. The smallest cross sections are always related to the lowest wave velocities, but only at low frequencies, the extensional or bar velocity of aluminum, given through Eq. (6) as $v_E = \sqrt{E/\rho} = 0.821 \times v_L$, with E as the isotropic Young's modulus of the transmitted material (here aluminum), is reached, see Fig. 3a. The bulk velocity is reached the earlier, the higher the used frequency, i.e. the lower the wavelength of the pulses sent through the samples, see Fig. 3b.

Tests on sample *set A2* (solid 'bar-like' aluminum boxes characterized by constant square-shaped cross sections with edge length of 3 mm, and by heights varying from 30 mm to 110 mm, see Table 5) reveal that longitudinal wave velocities increase with increasing frequency, unless they even reach, for $f = 10$ MHz and $f = 20$ MHz, the constant value of the bulk velocity of aluminum, $v_L = \sqrt{C_{1111}/\rho}$, see Fig. 4. At frequencies below 10 MHz, the longitudinal wave velocities increase with decreasing height, i.e. with decreasing slenderness of the bar-like specimens. Only at the lower frequencies, the most slender samples are transmitted by extensional waves (also called bar waves), and only at the higher frequencies, the least slender samples are transmitted by bulk waves, see Fig. 4a.

Tests on sample *set B* (solid 'plate-like' aluminum boxes characterized by constant square-shaped cross sections with edge length of 30 mm, and by heights/thicknesses varying from 0.5 mm to 30 mm, passing from plate-type to cubic shape, Table 5) reveal that propagation velocities are independent of height or thickness, being equal to the bulk velocity, and that they undergo large errors in case of small thicknesses in particular in combination with small frequencies (i.e. large wavelengths), see Fig. 5. These errors are in perfect agreement with our estimation of Section 3.2; i.e. for small thicknesses, the precision of the ultrasonic measurement system is lost.

The aforementioned test results referring to samples *sets A1*, *A2*, *B*, and *R*, can be cast into a consistent whole, by considering the normalized longitudinal wave velocities as 'altitudes' related to locations in the plane spanned by the dimensionless variables 'edge-length-over-height (a/h)' and 'height-over-wavelength (h/λ_L)', see Fig. 6. Fig. 6 refers to a 2D representation of the function (24), covering a range of the dimensionless variables a/h and h/λ_L, over four orders of magnitude. The lowest longitudinal wave velocities, matching the extensional velocity, are reached for slender samples (small a/h) when excited through relatively long wavelengths (large h/λ_L). Shorter wavelengths (smaller h/λ_L) seem to induce deformational constraints in the bar, being therefore transmitted by waves faster than the extensional wave. For less slender specimens (larger a/h) the bulk velocity is reached the
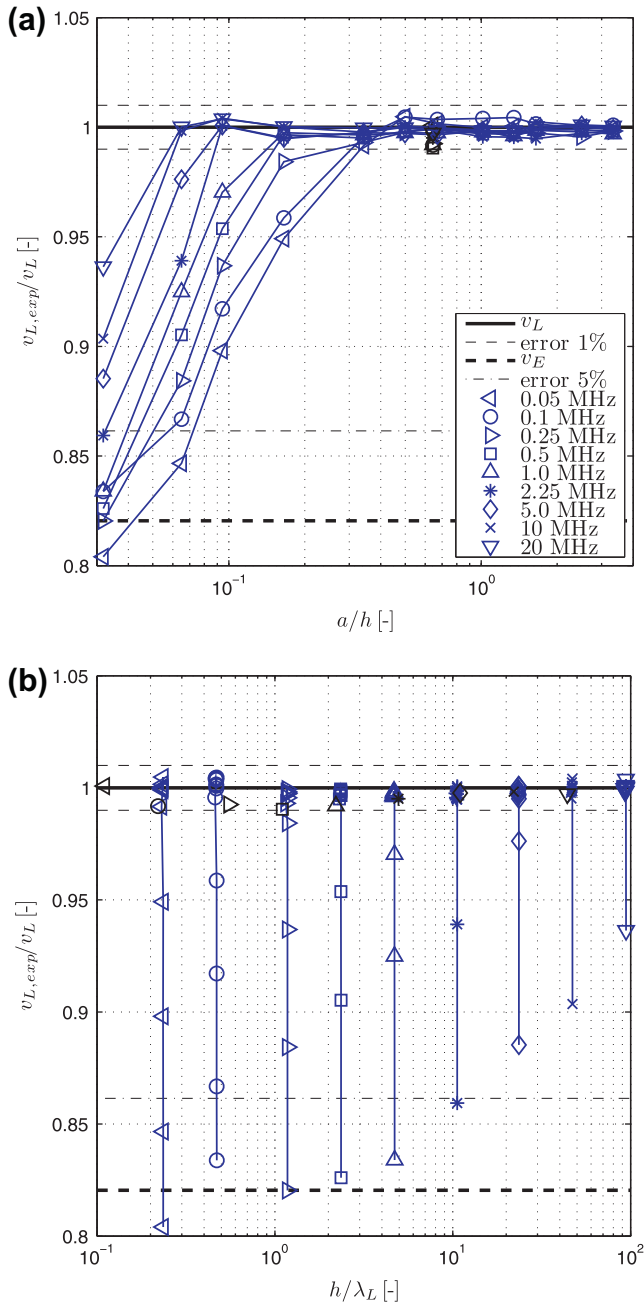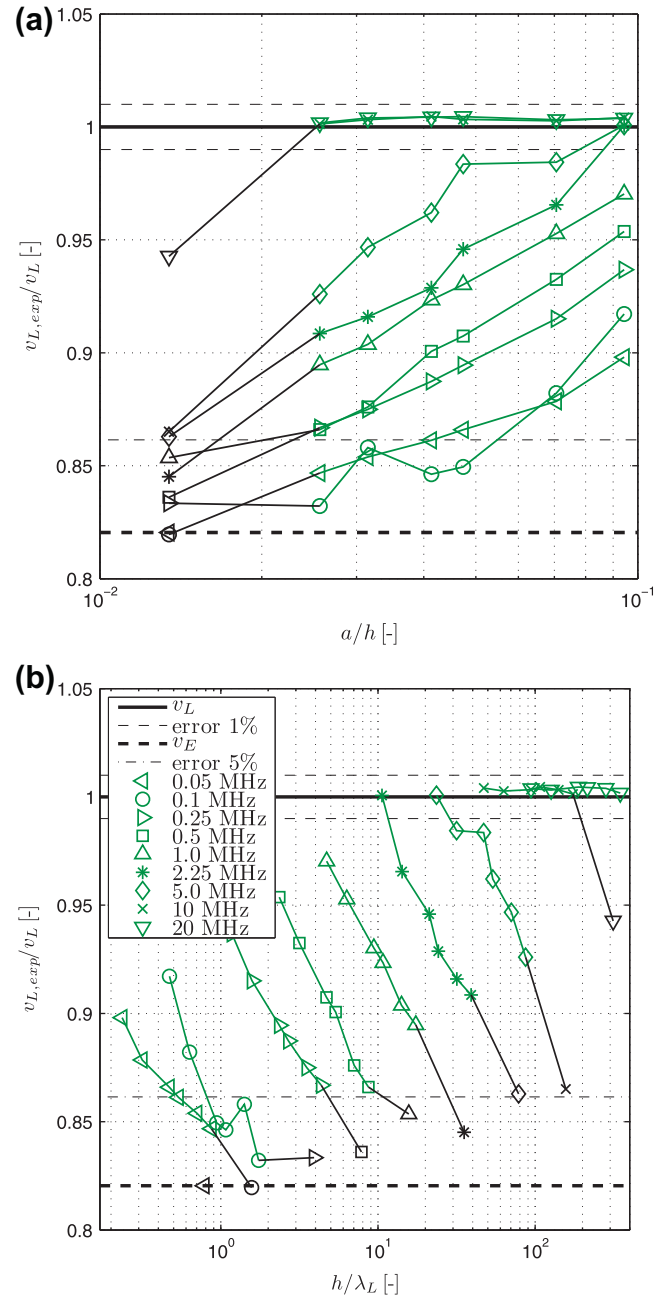
Fig. 3. Specimen *set A1, R-2* (according to Table 5): dependency of dimensionless longitudinal wave velocity ($v_{L,exp}/\sqrt{C_{1111}/\rho} = v_{L,exp}/v_L$), on (a) edge-length-over-height parameter (a/h), and on (b) height-over-wavelength parameter (h/λ_L); data points relating to the same h/λ_L-ratio are connected by solid lines.

Fig. 4. Specimen *set A2, R-1* (according to Table 5): dependency of dimensionless longitudinal wave velocity ($v_{L,exp}/\sqrt{C_{1111}/\rho} = v_{L,exp}/v_L$), on (a) edge-length-over-height parameter (a/h), and on (b) height-over-wavelength parameter (h/λ_L); data points relating to the same a/λ_L-ratio are connected by solid lines – remarkably, these lines are nearly parallel, even if a changes.

earlier, the smaller the relative wavelengths h/λ_L, i.e. the more of the aforementioned deformational constraints are imposed onto the sample. The corresponding boundary of the 'high plateau' in Fig. 6, related to bulk wave propagation, can be quantified by a linear relation in log (a/h) and log (h/λ_L), so that

bulk wave propagation $\forall \left(\dfrac{a}{h}\right), \ \left(\dfrac{h}{\lambda_L}\right)$

with $A \log \left(\dfrac{a}{h}\right) + B \log \left(\dfrac{h}{\lambda_L}\right) \leqslant 1,$ (25)

where $A = -1.426$ and $B = -0.530$ (see solid bold line in Fig. 6). The boundary for extensional wave propagation (with up to 5% error) is approximately parallel to this line (see dashed bold line in Fig. 6).

Beyond that boundary when tending towards $h/\lambda_L \to 0$, $a/h \to 0$ (i.e. for bar-shaped specimens excited by low-frequency signals), the bar-shaped specimens are transmitted by extensional waves,

extensional wave propagation $\forall \left(\dfrac{a}{h}\right), \ \left(\dfrac{h}{\lambda_L}\right)$

with $C \log \left(\dfrac{a}{h}\right) + D \log \left(\dfrac{h}{\lambda_L}\right) \geqslant 1,$ (26)

with $C = -0.776$ and $D = -0.282$. However, it is interesting to note that bar-shaped specimens (see vertical line at $a/h \approx 0.015$ in Fig. 6) may well be transmitted by bulk waves rather than by extensional waves. This is the case for wavelengths being smaller than the cross sectional length a (see $h/\lambda_L \approx 300$, $\lambda_L = 0.22\ a$, in Fig. 6),
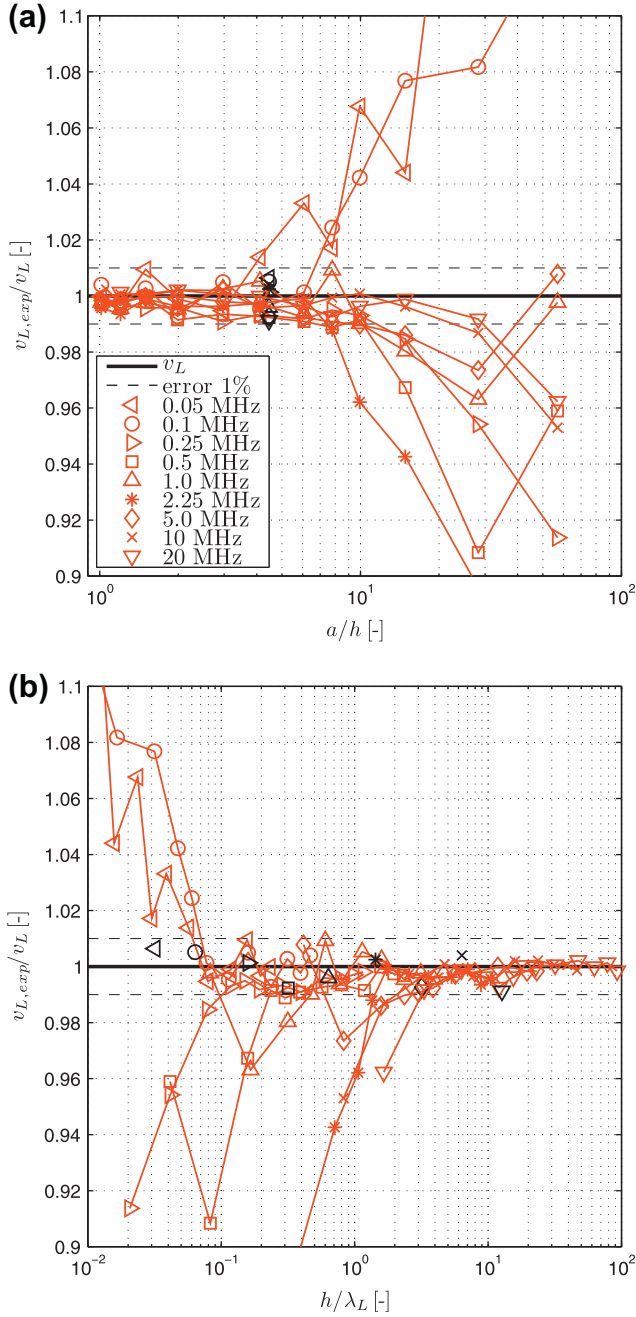
(a)

(b)

Fig. 5. Specimen *set B, R-3* (according to Table 5): dependency of dimensionless longitudinal wave velocity ($v_{L,exp}/\sqrt{C_{1111}/\rho} = v_{L,exp}/v_L$), on (a) edge-length-over-height parameter (a/h), and on (b) height-over-wavelength parameter (h/λ_L); data points relating to the same a/λ_L-ratio are connected by solid lines.

i.e. for high frequency signals propagating through our bar-type specimens. Our finding is consistent with that of Kolsky [47] who stated that the transition from extensional to bulk wave propagation through bar-type specimens starts at $\lambda_L \approx a$ ($h/\lambda_L \approx 100$, $a/h \approx 0.01$, in Fig. 6). For $\lambda_L \leqslant a$, the stress distribution across the specimen cross section is not any more uniform. This uniformity, however, would be the prerequisite for the validity of beam theory, here in the sense of Eq. (6). On the other side of the 'bulk velocity plateau' in Fig. 6, measurements of longitudinal waves through thin plates (large values of a/h) may become increasingly awkward and afflicted with errors, reflected by steep peaks and valleys adjacent to the 'high plateau' towards large edge-length-over-height ratios. Fig. 6 also suggest cubes to be an appropriate specimen shape for
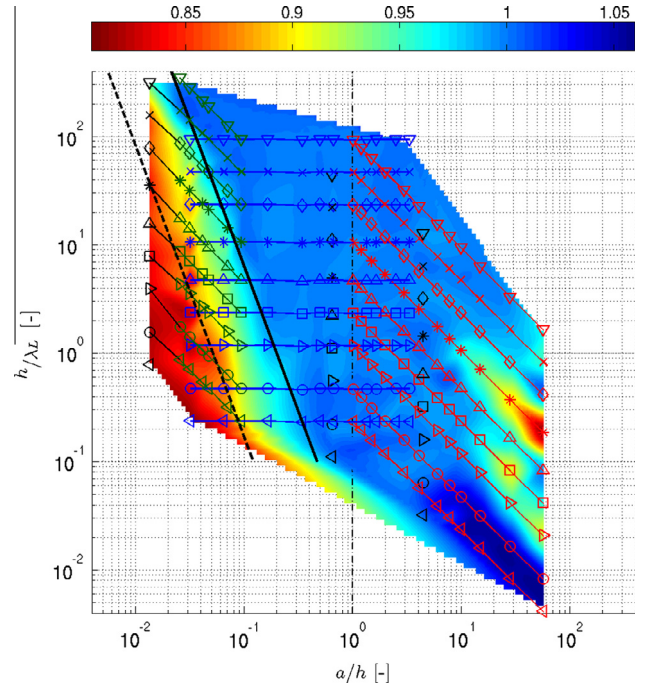
Fig. 6. Specimen *sets A, B, R* (according to Table 5): dependency of dimensionless longitudinal wave velocity ($v_{L,exp}/\sqrt{C_{1111}/\rho} = v_{L,exp}/v_L$), on specimen geometry (edge-length-over-height parameter a/h), and on wave frequency (in terms of height-over-wavelength parameter h/λ_L) – top view.

bulk wave velocity determination, especially for high frequencies ($a/h = 1$, $h/\lambda_L \to \infty$, see dash-dotted line in Fig. 6) when the wave is 'detecting' RVEs being much smaller than the specimen, while at low frequencies ($a/h = 1$, $h/\lambda_L \to 0$, see dash-dotted line in Fig. 6) specimens and RVEs are not well separated by scale and the bulk wave plateau in Fig. 6 becomes a little 'wavy'. The limit case $h/\lambda_L \to \infty$ is also preferable when aiming at bulk wave determination on platy specimens, see Fig. 6 for $a/h \approx 10 - 100$, while, for $h/\lambda_L < 1$, measurements on platy specimens may be afflicted with large measurement errors (see Fig. 6). This is consistent with the theoretical error propagation analysis in Section 3.2, Table 4.

The elastodynamic analogon to (21) for shear waves reads as:

$$v_T = \sqrt{\frac{C_{1212}}{\rho}}, \tag{27}$$

with v_T as the ('bulk') shear wave velocity, and with C_{1212} as the shear stiffness component of the elasticity tensor (being equal to the shear modulus G), compare $(4)_2$. Considerations analogous to (22)–(24) yield the dimensionless shear wave velocity as:

$$\frac{v_{T,exp}}{\sqrt{C_{1212}/\rho}} = \frac{v_{T,exp}}{v_T} = \mathscr{G}\left(\frac{a}{h}, \frac{h}{\lambda_T}\right). \tag{28}$$

Function $\mathscr{G}$ is a 'high plateau' at altitude '1' (reflecting the fact that there do not exist 'bar-type' shear waves), and is only bounded by 'peaks' and 'valleys' related to the technical limitations of the employed measurement system (described in Section 3.1), see Fig. 7. In any case, sufficiently high frequencies and corresponding short wavelengths ($h/\lambda_T > 20$) guarantee non-dispersive shear wave propagation, for all types of investigated sample shapes, from bars to plates.

7. Microstructure-specific wave propagation

While the last section was devoted to the case of the long-wavelength-limit, where the wavelengths are significantly larger than the material volumes (see right-hand side of Eq. (1)), we now discuss propagation velocities of waves spanning the entire range from wavelengths being much larger than the material volumes of porous media, via such being of the size of such porous material volumes or of the size of the microstructural entities (pores), to finally such being even smaller than the microstructural entities (pores). As described in Section 4, we study the microstructure 'cylindrical pores in solid (isotropic) aluminum matrix' [with hexagonal (and hence transversely isotropic) instead of isotropic properties], which, according to Drugan and Willis [20], is an extreme case where the microstructural entities start to have a discernable influence already at relatively large wavelengths. Accordingly, Eq. (24) now refers to very small waves traveling directly through the isotropic aluminum matrix, without interference with the cylindrical pores. However, the experimentally determined velocities are now functions of two additional arguments, pore diameter d and porosity φ, so that the dimensionless function (24) needs to be extended to the format:

$$\frac{v_{L,exp}}{v_L} = \mathscr{H}\left(\frac{a}{\lambda_L}, \frac{h}{\lambda_L}, \frac{d}{\lambda_L}, \varphi\right). \tag{29}$$

In principle, we could have also introduced pore center distance e in Fig. 1 as the measure for the microheterogeneity size, see Table 6 for relations between e and pore diameter d. While the corresponding results on the effect of microheterogeneities on wave propagation, as reported herein, would remain independent of the choice of e versus d, the pore size d is the more common choice in the open literature [56]. In order to keep the discussions in a tractable size, we now consider only ranges where our previous study on sample sizes did not suggest influences of a/h and h/λ_L on v_{exp}/v_L, i.e. we restrict ourselves to the 'high plateau'-region of Fig. 6. In other words, we study microstructure-specific wave propagation, independent of sample geometry-specific wave propagation. Accordingly, we consider the dimensionless functions:

$$\frac{v_{L,exp}}{\sqrt{C_{1111}/\rho}} = \frac{v_{L,exp}}{v_L} = \mathscr{I}\left(\frac{d}{\lambda_L}, \varphi\right)$$

$$\text{and} \quad \frac{v_{T,exp}}{\sqrt{C_{1212}/\rho}} = \frac{v_{T,exp}}{v_T} = \mathscr{J}\left(\frac{d}{\lambda_T}, \varphi\right), \tag{30}$$

where $(30)_2$ relates to transverse waves through specimens which do not evoke measurement errors (see 'high plateau'-region in Fig. 7). In order to elucidate the features of $\mathscr{I}$ and $\mathscr{J}$, we evaluate the test results of sample set C (mainly cubic samples with cylindrical pores in different configurations, defined in Fig. 1b and Table 6). Because of the transversely isotropic nature of the specimen with the principle material directions 1, 2, and 3 (see Fig. 1), functions $\mathscr{I}$ and $\mathscr{J}$ additionally depend on the propagation direction. Accordingly, we discuss in the following three functions $\mathscr{I}$, $\mathscr{I}_1$, $\mathscr{I}_2$, $\mathscr{I}_3$, related to longitudinal wave propagation velocities $v_{1,1,exp}$, $v_{2,2,exp}$, and $v_{3,3,exp}$, respectively (the repeated index indicates coincidence of the propagation and polarization directions in longitudinal waves), and six functions $\mathscr{J}$, $\mathscr{J}_{i,j}$, $i \neq j$, $i,j = 1, 2, 3$, related to transverse wave velocities $v_{i,j,exp}$ with propagation direction i and polarization direction j, $i \neq j$. 3D representations of functions $\mathscr{I}_1$ (see Fig. 8a; velocity referring to longitudinal normal stiffness), average of $\mathscr{I}_2$ and $\mathscr{I}_3$ (see Fig. 8b; velocities referring to (transverse) normal stiffness in isotropic plane), average of functions $\mathscr{I}_{1,3}$, $\mathscr{I}_{3,1}$, $\mathscr{I}_{2,3}$, and $\mathscr{I}_{3,2}$ (see Fig. 9a; velocities referring to longitudinal shear stiffness), and average of functions $\mathscr{I}_{1,2}$, $\mathscr{I}_{2,1}$ (see Fig. 9b; velocities referring to (transverse) shear stiffness in the isotropic plane) show the dependency of the bulk wave velocity on both the porosity φ and the pore-diameter-over-wavelength parameter d/λ_i.

Generally, longitudinal wave velocities increase with increasing pore diameter-over-wavelength ratio d/λ_L, with two limit cases:

1. For large values of this ratio d/λ_L, the longitudinal waves traveling in the cylindrical pore direction reach the bulk velocity related to pure aluminum alloy (see Fig. 10a); in other words, the waves [with wavelengths shorter than the pore diameters, i.e. for $d/\lambda_L \approx 2$ at higher porosities; but even for $d/\lambda_L \approx 0.04$ at low porosities] propagate through the solid aluminum matrix, while not interacting with the cylindrical pores (see Fig. 10a).
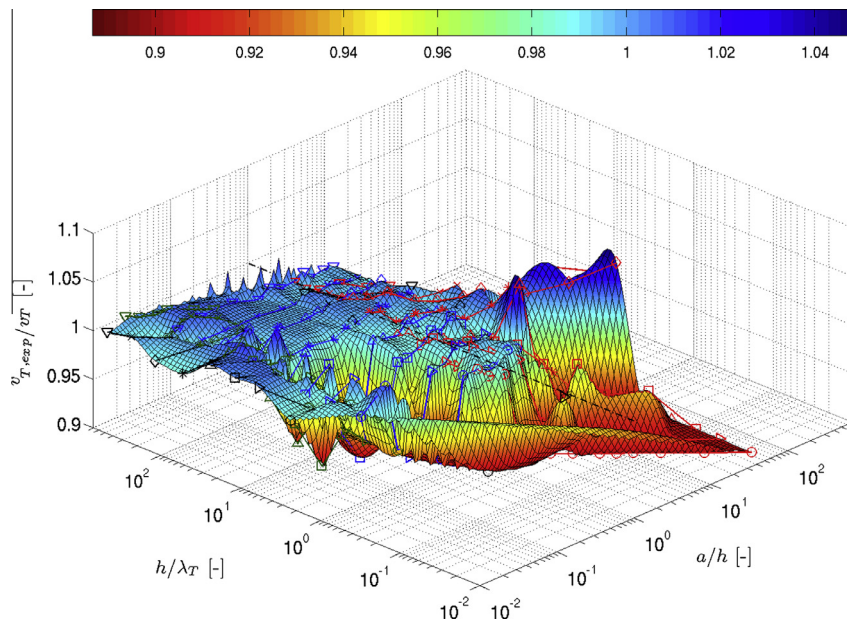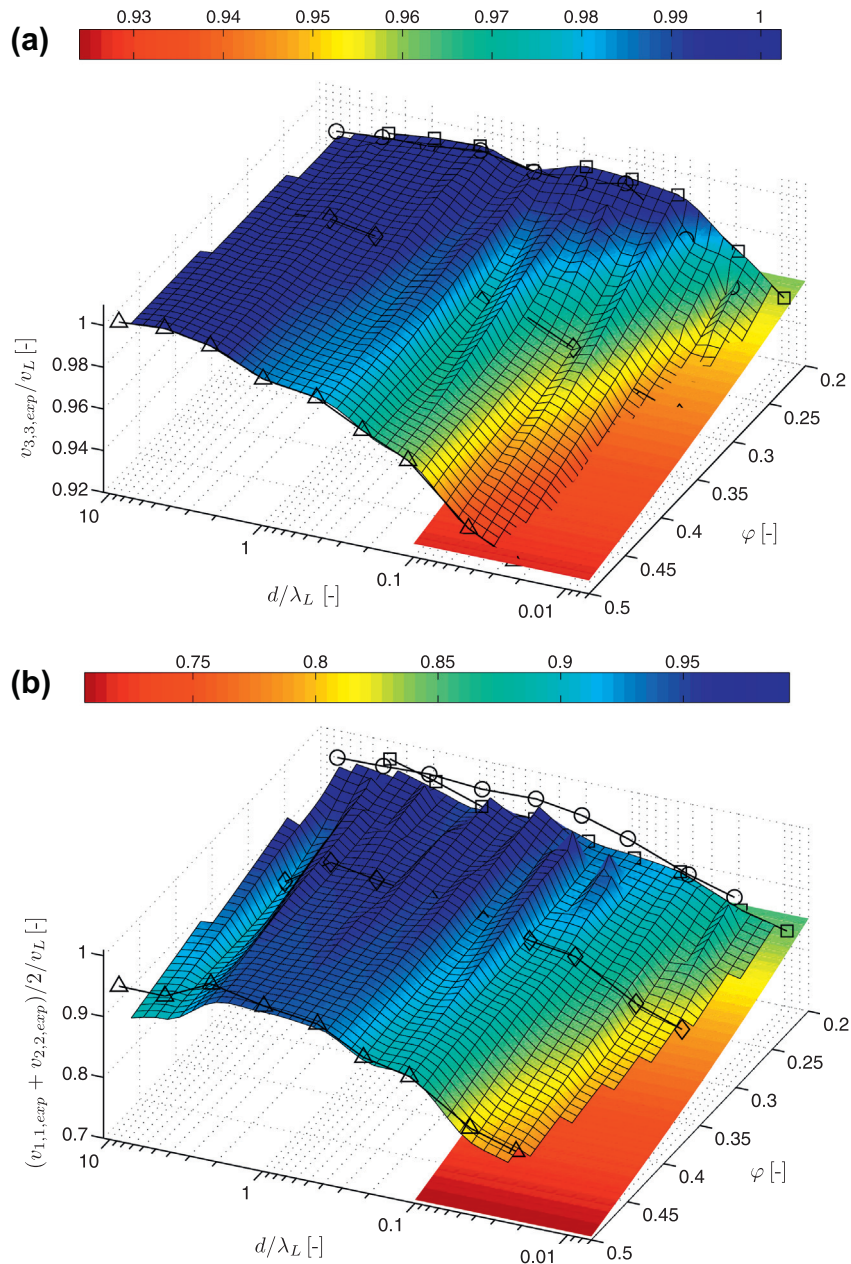

Fig. 7. Specimen sets A, B, R (according to Table 5): dependency of dimensionless transverse wave velocity ($v_{T,exp}/\sqrt{C_{1212}/\rho} = v_{T,exp}/v_T$), on specimen geometry (edge-length-over-height parameter a/h), and on wave frequency (in terms of height-over-wavelength parameter h/λ_T).
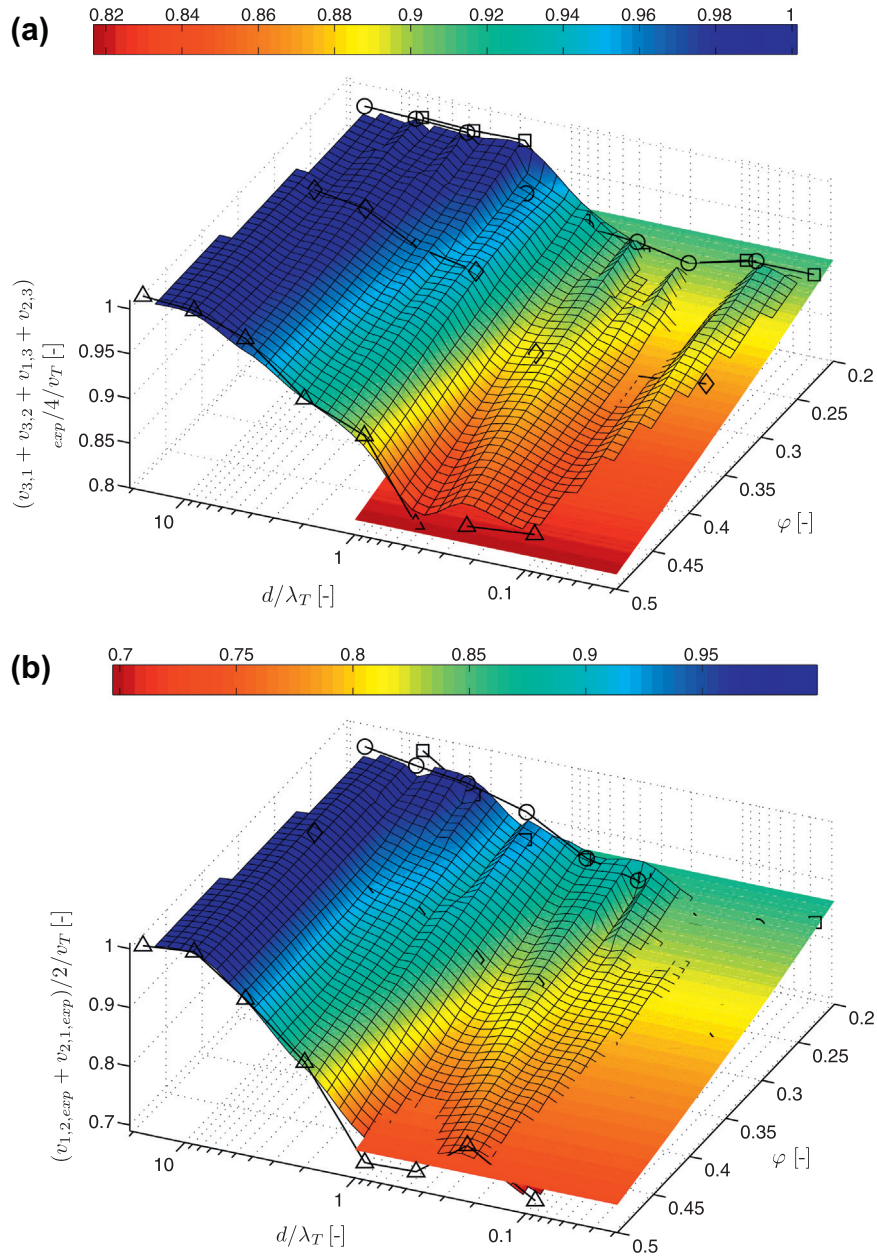
Fig. 8. Dependency of normalized longitudinal ultrasonic velocities in transversal isotropic media in (a) longitudinal $[v_{1,1,exp}/v_L]$ and (b) transverse $[(v_{2,2,exp} + v_{3,3,exp})/2/v_L]$ direction, on d/λ_L and φ [model predictions according to Hashin and Rosen [29] and Hlavacek [35], respectively, shown for reference in (a) and (b), respectively (surfaces without gridlines); for details see Section 8 and Appendix A].

This is also true for the longitudinal waves traveling perpendicular to the cylindrical pore direction, within the specimens which exhibit the lower porosity (see lines labeled by circles and squares in Fig. 10b and c). At higher porosities, the waves start to interact with the pores, being scattered at the pore surfaces. None of the traveling waves can take the shortest path through the specimen, the wave paths become, so to speak, 'more tortuous' – this leads to longer times of flight and to a lower velocity measured along the shortest distance between the opposite faces of the considered specimen (see lines labeled by diamonds and triangles in Fig. 10b and c). This tortuosity effect is more pronounced in the direction 2 (characterized by a zig-zag-type positioning of pores) than in the direction 1 (where straight (but only very thin) wall paths exist between the specimen faces, which, inspite of their straightness, cannot

provide a tortuosity-free propagation of longitudinal waves, see Fig. 1a and compare Fig. 10c and b). The tortuosity effect may be also enhanced by geometry-induced attenuation.

2. For small values of d/λ_L, the waves reach the bulk velocity related to the porous media through which they travel. These bulk velocities can be reasonably predicted by random homogenization theory (continuum micromechanics), corresponding predictions are indicated in Fig. 10 (while we refer to the next section for mathematical expressions related to different micromechanical models). This good predictability shows that the waves (with wavelengths being considerably larger than the pore diameter, i.e. tending towards the long-wavelength-limit) 'feel' the entire porous medium, consisting of both the solid aluminum matrix and the cylindrical air pores. In accordance with theoretical micromechanics, the bulk velocities through the

Fig. 9. Dependency of normalized transverse ultrasonic velocities in transversal isotropic media in (a) longitudinal [$(v_{3,1,exp} + v_{3,2,exp} + v_{1,3,exp} + v_{2,3,exp})/4/v_T$] and (b) transverse [$(v_{1,2,exp} + v_{2,1,exp})/2/v_T$] direction, on d/λ_T and φ [predictions of Mori–Tanaka-type model shown for reference (surfaces without gridlines); for details see Section 8 and Appendix A].

considered specimens are the smaller the higher the porosity, and they are smaller in the transversely isotropic directions than in the anisotropic direction (that of the cylindrical pores). Still, it should be noted that for constant pore diameter d and constant frequency f, λ_L is smaller in the transverse directions (due to lower propagation velocities in these directions). At higher porosities, this smaller λ_L may not feel any more the porous medium in the sense of theoretical micromechanics, see Fig. 10b and c, for φ = 48.7%. Also, the implication of hexagonal microstructures exhibiting transversely isotropic material behavior [33], i.e. $v_{2,2} = v_{3,3}$ in Fig. 10b and c, is experimentally reflected only at sufficiently large wavelengths. Otherwise, the continuous straight paths between the pores, oriented in direction 1 (see Fig. 1), lead to overestimation of the effective porous medium-related longitudinal wave velocity.

Similar trends are observed for transverse waves traveling through the porous specimens of *set C* (see Fig. 11). However, two major differences with respect to the longitudinal waves are noted: (i) the 'tortuosity effect' for short wavelengths is negligible, so that all waves reach, for large d/λ_T, the shear wave velocity related to the aluminum matrix (see Fig. 11), (ii) for diminishing d/λ_T below 1, the effective (long-wavelength-limit-related) transverse velocities related to the porous medium are reached significantly faster than it is the case for longitudinal waves. This effect is particularly characteristic for transverse velocities in the cylindrical pore direction, $v_{3,1}$ and $v_{1,3}$ (see Fig. 11a and b). For small d/λ_T, when the separation-of-scales requirement (1) is fulfilled, the experimental measurements show the theoretically expected symmetries $v_{1,3} = v_{3,1} = v_{2,3} = v_{3,2}$ and $v_{1,2} = v_{2,1}$ (Fig. 11). When leaving this limit, wave propagation is less influenced by a change
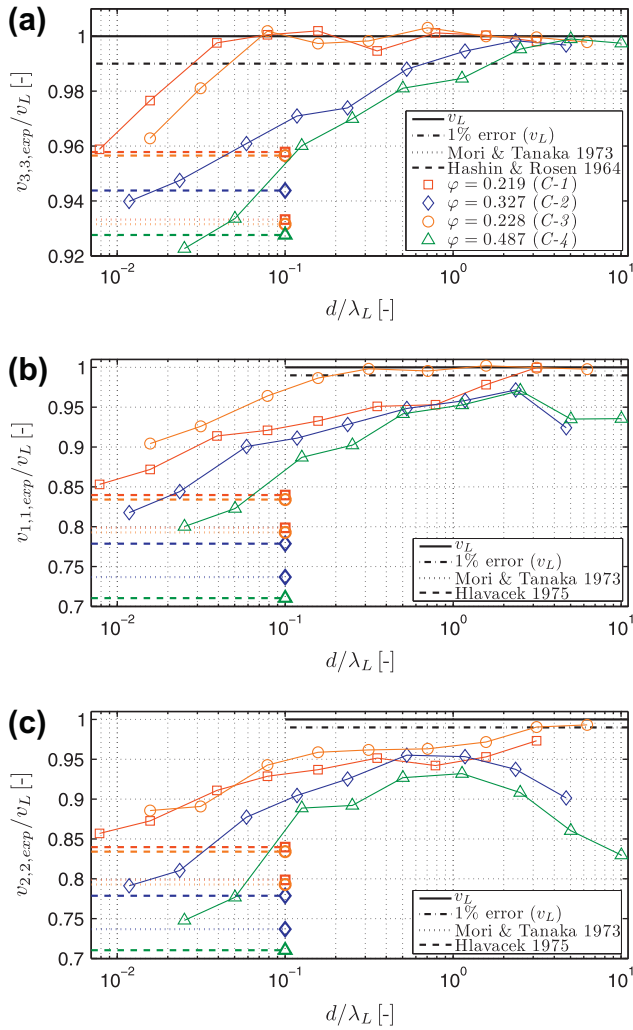
Fig. 10. Specimen *set C* (transversely isotropic, porous specimens): Influence of pore diameter-over-wavelength ratio (d/λ_L), on longitudinal dimensionless wave velocities in (a) anisotropic direction 3 (orientation of cylindrical pores), $v_{3,3,exp}$, and in (b) and (c) directions within isotropic plane, $v_{1,1,exp}$, $v_{2,2,exp}$ (for definition of directions 1 and 2, see Fig. 1; micromechanical models are described in Section 8 and Appendix A).

of polarization direction only (compare Fig. 11a and b), as compared to a change in both polarization and propagation directions (compare Fig. 11a and c as well as Fig. 11b and d).

8. Waves characterizing representative material volumes – comparison to theoretical micromechanics

For small d/λ, the separation-of-scales requirement (1) is fulfilled and the ultrasonic waves characterize a representative volume element of the transversely isotropic porous aluminum material of specimen *set C*. It is instructive to compare these experimental results (Figs. 8–11) to mathematical models from the micromechanics field, as to elucidate the relevance of both the employed experimental technique and the theories developed over half a century. For this purpose we have evaluated the theoretical predictions of four different mathematical models relating pore morphology and volume fraction to elastic stiffness tensors of the investigated porous materials (which are related, via (2) and (3), to the long-wavelength-limit-related propagation velocities $v_{i,j}$, $i, j = 1, 2, 3$): (i) Hashin and Rosen's [29] variational method for effective elastic properties of a (isotropic) solid matrix

perforated by randomly distributed cylindrical pores [29], (ii) Hlavacek's [35] Hamilton's principle-based method for effective elastic properties of a (isotropic) solid matrix perforated by hexagonally arranged pores [35], (iii) Eshelby [23] problem-based, Mori–Tanaka-type estimation of effective elastic properties of a solid matrix with randomly distributed pores, in the context or random homogenization theory (mean field homogenization) or continuum micromechanics [63,7,92], and (iv) the unit cell method for effective elastic properties of periodic media [81,9,54], applied to an array of periodically arranged cylindrical pores in a solid matrix. Details on these micromechanical models can be found in Appendix A. For discussion of these models with respect to our experiments, we employ the following error measures

$$\delta = \frac{1}{k}\sum_{n=1}^{k}\frac{C_{ijij}^{hom}(n) - C_{ijij}^{exp}(n)}{C_{ijij}^{exp}(n)} = \frac{1}{k}\sum_{n=1}^{k}\delta_n \quad \text{and} \quad s$$

$$= \sqrt{\frac{1}{k-1}\sum_{n=1}^{k}(\delta_n - \delta)^2}, \tag{31}$$

where $k = 4$ for C_{3333} and C_{1212}, $k = 8$ for C_{1111} and C_{1313}, δ_n is the relative error of each model stiffness prediction, and δ and s are the mean and standard deviations of these errors, respectively.

As regards normal stiffnesses (Fig. 12), the experimental values for the longitudinal stiffness component C_{3333} agree almost perfectly with Hashin and Rosen's micromechanical estimates (relative error of $0.1 \pm 1.1\%$, see thin dash-dotted line and upright triangular marker in Fig. 12), while these values lie slightly above the micromechanical predictions of the Hlavacek model, the Mori–Tanaka-type random homogenization result, and our unit cell approach (relative errors of $-4.5 \pm 0.6\%$, $-5.5 \pm 0.6\%$, and $-5.3 \pm 0.7\%$, respectively; see thin dotted and thick dashed lines, as well as square and upright triangular markers in Fig. 12), and they are larger for the tests in specimen C-3 (with $\varphi = 22.8\%$ and larger pores) than for C-1 (with $\varphi = 21.9\%$ and smaller pores). The latter observation reflects the effectively larger RVE of C-3, when compared to that of C-1. The experimental values for the transverse normal stiffness component C_{1111} lie slightly above the predictions of the Hlavacek model (relative error of $-9.6 \pm 6.3\%$, see thin dashed line and horizontal triangles in Fig. 12), and are even more distant from the Mori–Tanaka-type and unit cell predictions (relative errors of $-18.9 \pm 6.1\%$ and $-20.0 \pm 7.4\%$, respectively; see thick solid line, as well as circular and horizontal triangular markers in Fig. 12). The aforementioned deviations between experimental values and micromechanical model predictions are the more pronounced the higher the porosity of the investigated specimens. The experimental values for the plane strain bulk modulus in the isotropic transverse plane, $K_{12} = C_{1111} - C_{1212}$, almost perfectly agree with Hashin and Rosen's micromechanical estimates (relative error of $-3.4 \pm 8.2\%$, see thin solid line and diamond as well as upside-down triangle markers in Fig. 12).

As regards shear stiffnesses (Fig. 13), the experimental values for the longitudinal shear stiffness component C_{1313} agree almost perfectly with the Mori–Tanaka-type micromechanical estimates (relative error of $-1.5 \pm 3.0\%$, see thick dashed line and horizontal triangular markers in Fig. 13), as well as with those of our unit cell models (relative error $-1.3 \pm 3.1\%$, see circular and horizontal triangular markers in Fig. 13), with those of Hlavacek's 1975 model (relative error of $-0.2 \pm 3.3\%$, see thin dotted line and horizontal triangular markers in Fig. 13), and with those of Hashin and Rosen's 1964 model (relative error of $-1.5 \pm 3.0\%$, see thin dash-dotted line and horizontal triangular markers in Fig. 13). The experimental values for the transverse inplane shear stiffness C_{1212} agree almost perfectly with the Mori–Tanaka-type stiffness estimate (relative error of $2.5 \pm 2.0\%$, see thick solid line and upright triangular markers in Fig. 13), and almost as well with
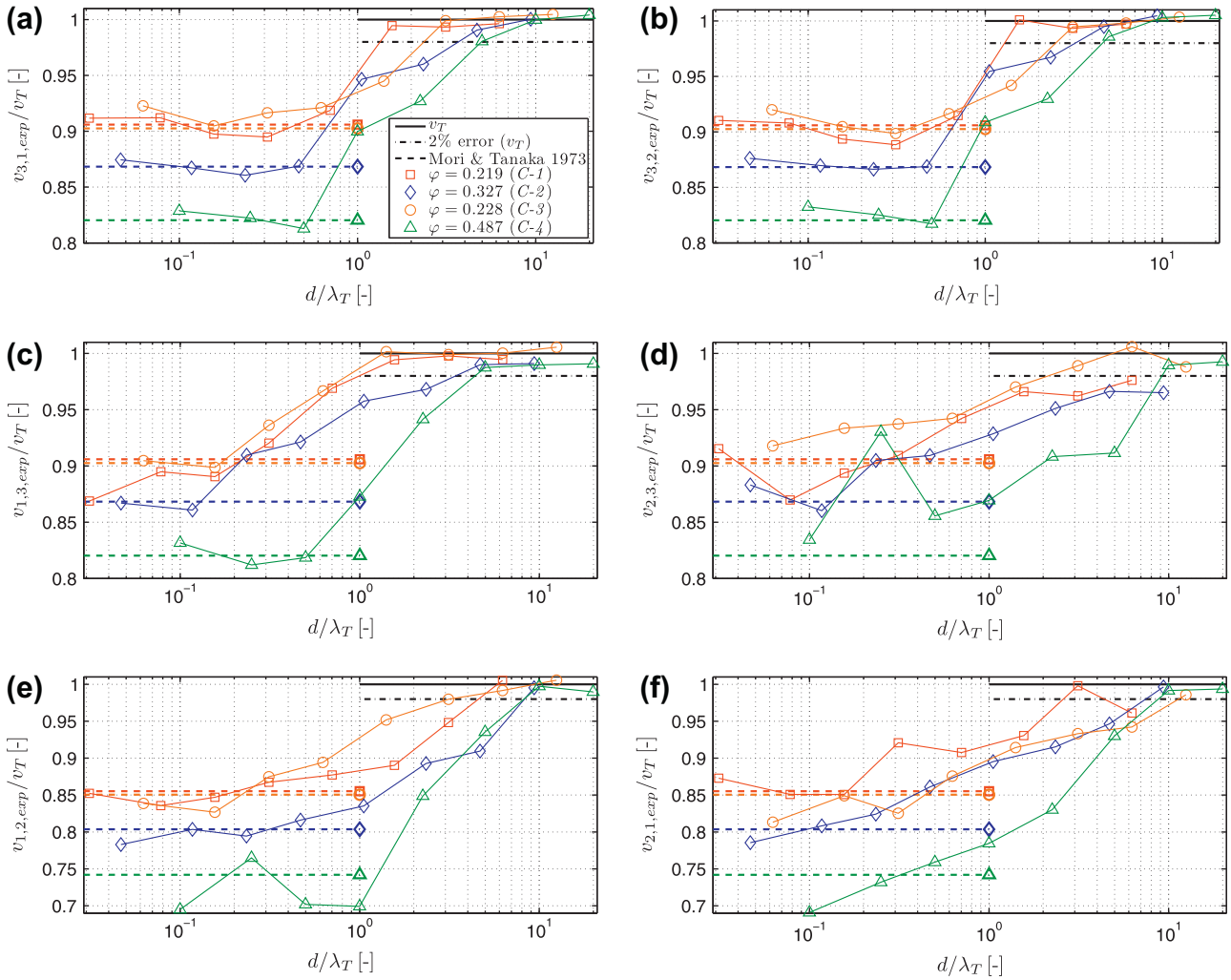
Fig. 11. Specimen *set C* (transversely isotropic, porous specimens): influence of pore diameter-over-wavelength ratio (d/λ_T), on transverse dimensionless wave velocities in (a) and (b) anisotropic direction 3 (orientation of cylindrical pores), $v_{3,1,exp}$ and $v_{3,2,exp}$, in propagation directions within the isotropic plane with (c) and (d) polarization directions perpendicular to this plane, $v_{1,3,exp}$ and $v_{2,3,exp}$, and with (e) and (f) polarization directions within this plane, $v_{1,2,exp}$ and $v_{2,1,exp}$ (for definition of directions 1 and 2, see Fig. 1; micromechanical models are detailed in Section 8 and Appendix A).
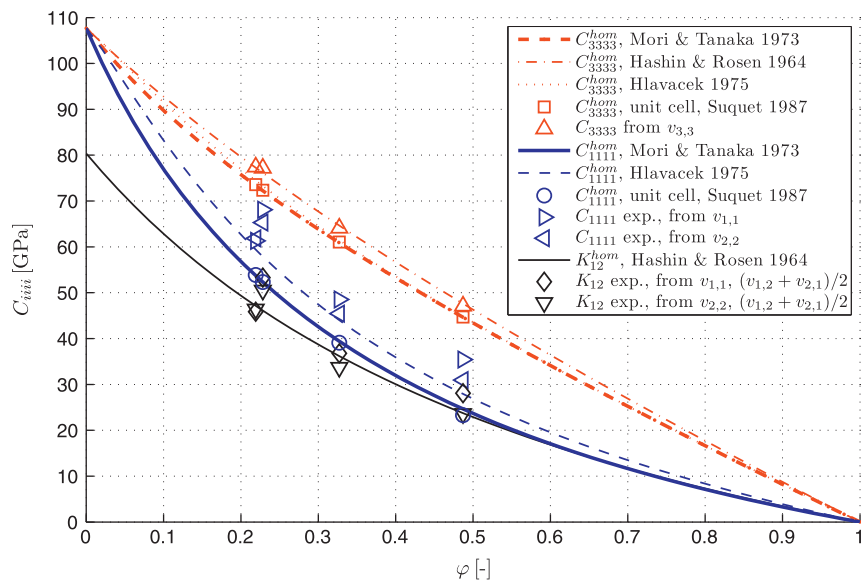
Fig. 12. Normal stiffness tensor components (C_{3333}, $C_{1111} = C_{2222}$) as function of volume fraction of pores φ – comparison of ultrasonic measurements ($f = 50$ kHz) with hexagonal array models ([35] and unit cell according to Fig. 1c) and random array models [29,63].
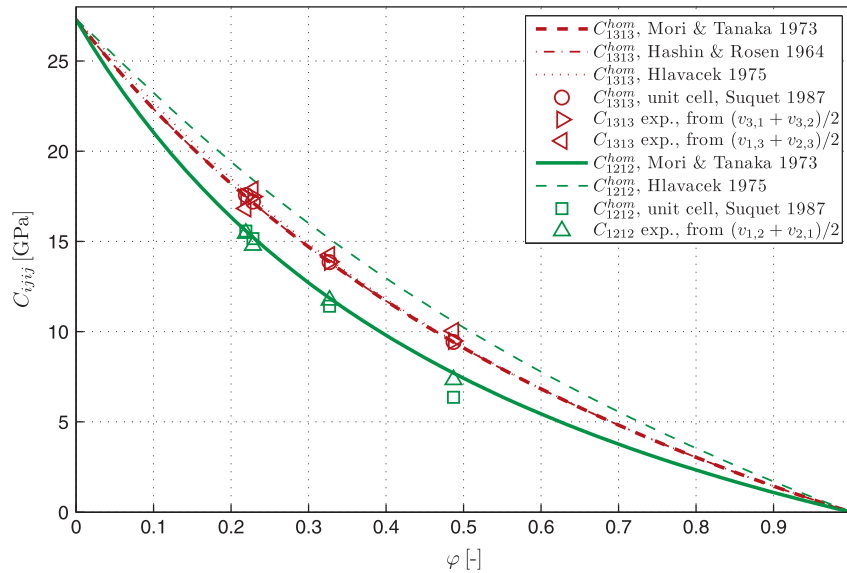
Fig. 13. Shear stiffness tensor components ($C_{1313} = C_{2323}$, C_{1212}) as function of volume fraction of pores φ – comparison of ultrasonic measurements (average of results from f = 100, 250, and 500 kHz were used) with hexagonal array models ([35] and unit cell according to Fig. 1c) and random array models [29,63].

the predictions from our unit cell approach (relative error of $-3.2 \pm 7.1\%$, see square and upright triangular markers in Fig. 13), while Hlavacek's 1975 model grossly overestimates the experimentally determined shear stiffnesses (relative error of $29.7 \pm 10.1\%$, see thin dashed line and upright triangular markers in Fig. 13).

9. Conclusion – operational rules

In this paper, we have identified requirements on sample geometry and porosity, for reliable measurement of elastic properties by means of ultrasonic contact pulse transmission: firstly, we quantified ranges of dimensions of box-shaped samples and pulse frequencies, where non-dispersive, i.e. frequency-independent, bulk or bar waves allow for direct determination of the samples' elasticity; as well as the dispersive transition zones inbetween. Secondly, we determined limits of the pore diameter-over-wavelength ratio in transversely isotropic porous samples with cylindrical pores: below the short-wavelength limit, the waves 'detect' the elasticity of the material between the pores, and above the long-wavelength limit, the waves 'detect' the overall porous medium. Inbetween, we observe a dispersive transition zone, the size of which is comparable to transition regions in other (two-phase) materials [60,42,80,27] and which is increasing with increasing porosity and with decreasing direction-dependent wave propagation velocity. Conclusively, our experimental and theoretical results allow for formulation of the following operational rules:

– As to minimize measurement errors, use of bar-type, cubic, and thick plate-type specimens is recommended, while thin plates, especially in combination with low frequencies, should be avoided (based on results from Sections 5 and 6). Under these conditions, ultrasonic measurements are a precise means to determine diagonal (normal and shear) stiffness components, while they give (by a factor of two) less precise values for off-diagonal (Poisson-effect-related) stiffness components (Section 5).
– As to guarantee extensional (or bar) wave propagation along bar-type specimens, the latter need to exhibit slenderness ratios of 20 or larger, if the wavelength is equal to the travel distance of the pulse. For longer wavelengths, the required slenderness decreases, while it increases when employing shorter wavelengths (this requirement is quantified through Eq. (26)).

– As to guarantee bulk wave propagation, specimens with a slenderness ratio of 5 or smaller need to be used, if the wavelength is equal to the travel distance of the pulse. For longer wavelengths, the required slenderness decreases, while it increases when employing shorter wavelengths (quantified through Eq. (25)).
– As to guarantee normal stiffness determination of transversely isotropic porous media with aligned cylindrical pores (long-wavelength-limit), the pore dimension-over-wavelength ratio needs to be smaller than 0.01. As to guarantee shear stiffness determination of transversely isotropic porous media with aligned cylindrical pores (long-wavelength-limit), the pore dimension-over-wavelength ratio needs to be smaller than 0.1. As to guarantee normal stiffness determination of the solid material between the aforementioned pores (short-wavelength-limit), the pore dimension-over-wavelength ratio needs to be larger than 1. As to guarantee shear stiffness determination of the solid material between the aforementioned pores (short-wavelength-limit), the pore dimension-over-wavelength ratio needs to be larger than 10 (these rules are based on the results of Section 7).
– As to predict the elasticity of transversely isotropic porous media (long-wavelength-limit), Mori–Tanaka, Hashin–Rosen, and unit cell micromechanical models are suitable. This is particularly true for shear stiffnesses, for normal stiffnesses in cylindrical pore direction, and for plain strain bulk moduli. In contrast, experimentally determined normal stiffnesses perpendicular to the cylindrical pore direction are better predicted by Hlavacek's micromechanical model (Section 8).

Appendix A. Micromechanics models – background

A.1. Variational method for effective elastic properties of a solid matrix perforated by randomly distributed parallel cylindrical pores – Hashin and Rosen [29]

Hashin and Rosen [29] aim at estimating the elastic behavior of a porous material consisting of a solid matrix perforated by parallel, randomly distributed, coated cylindrical pores – which we here specialize for non-coated pores. Therefore, a representative volume element of such a porous material is considered, and subjected to homogeneous boundary conditions, be it in terms of macroscopic stresses or strains. In order to estimate the elastic response of such an RVE to these boundary conditions, single cylinders ('composite cylinders') consisting of a cylindrical pore and surrounding material are subjected to homogeneous stress boundary conditions (this leads to a lower bound for the effective (homogenized) stiffness), and to homogeneous strain boundary conditions (this leads to an upper bound for the effective (homogenized) stiffness). In case of a random arrangement of pores, the entire material space is filled up with the composite cylinders, so that the upper and the lower bounds coincide. Then, the effective (homogenized) Young's modulus E_3^{hom} and the plain strain bulk modulus in the isotropic transverse plane $K_{12}^{hom} = C_{1111}^{hom} - C_{1212}^{hom}$ are given as:

$$E_3^{hom} = E(1-\varphi) \quad \text{and} \quad K_{12}^{hom} = (C_{1111} - C_{1212})\frac{2v(1-\varphi)}{2v+\varphi}, \quad (32)$$

respectively, where E, v, C_{1111}, and C_{1212} are the elastic constants of the isotropic matrix (in our case aluminum alloy, see Table 7), and φ denotes the porosity (see Table 6). The corresponding longitudinal (normal and shear) stiffness components, C_{3333}^{hom} and $C_{1313}^{hom} = C_{2323}^{hom}$ read as:

$$C_{3333}^{hom} = E_3^{hom} + 4v^2 K_{12}^{hom} \quad \text{and} \quad C_{1313}^{hom} = C_{1212}\frac{1-\varphi}{1+\varphi}. \quad (33)$$

A.2. Hamilton's principle-based method for effective elastic properties of a solid matrix perforated by hexagonally arranged, parallel cylindrical pores – Hlavacek [35]

Hlavacek [35] developed an effective stiffness theory for a hexagonal array of (isotropic) cylindrical inclusions embedded in a (isotropic) matrix (which we here specialize for pore inclusions), by assuming specific (continuous) displacement distributions within the composite, and by relating them to some 'gross–displacements', which, via Hamilton's principle in combination with the elastic and mass properties of the solid matrix and with the porosity, gives access to phase velocities of waves propagating in the lowest mode through the porous medium. Comparing these expressions for the phase velocities with those obtained from elastodynamics of the homogenized medium, yields the effective (homogenized) elastic properties of the porous medium as

$$C_{1111}^{hom} = \left(q + p(3q+1) - p^2 \right.$$
$$\left. \times \frac{2pq(3q+1)(q+1) - \varphi(3q+1)(q-1) - \varphi q(q+1)^2}{[p(q+1)-\varphi][2pq-\varphi(q-1)]}\right)C_{1212}, \quad (34)$$

$$C_{3333}^{hom} = \left(q(1-\varphi) - \frac{\varphi^2 r^2}{2pq - \varphi(q-1)}\right)C_{1212}, \quad (35)$$

$$C_{1212}^{hom} = \left(1 + p(q+1) - \frac{p^2(q+1)^2}{p(q+1)-\varphi}\right)C_{1212}, \quad (36)$$

$$C_{1313}^{hom} = \left(\frac{4p - \varphi(4p+1)}{4p - \varphi}\right)C_{1212}, \quad (37)$$

with the abbreviations p, q, and r being defined as:

$$p = -\frac{\varphi \log(\varphi)}{8(1-\sqrt{\varphi})^2}, \quad q = 2\frac{1-v}{1-2v}, \quad \text{and} \quad r = 2\frac{v}{1-2v}. \quad (38)$$

A.3. Mean-field homogenization method (Mori–Tanaka estimate) for effective elastic properties of a solid matrix perforated by randomly distributed, parallel cylindrical pores – [23,63,7]

A representative volume element (RVE) of the above mentioned porous material is considered, and subjected to homogeneous boundary conditions, be it in terms of macroscopic stresses or strains. These boundary conditions imply that the spatial average of the equilibrated microstresses within the RVE are equal to the homogeneous (macroscopic) strains (strain average rule), and the spatial average of the kinematically admissible microstrains within the RVE are equal to the homogeneous (macroscopic) stresses (stress average rule). Then, the strain average rule is combined with Eshelby's 1957 matrix inclusion problem relating the strains in a cylindrical pore to those subjected to the remote boundary of an infinite matrix surrounding this pore, yielding relations between the remote auxiliary strains and the macroscopic, RVE-related strains. The resulting concentration relations between RVE-related homogeneous strains and pore and matrix strains, together with the stress average rule, give finally access to the homogenized elastic properties, in the form [92]

$$\mathbb{C}^{hom} = (1-\varphi)\mathbb{C} : [(1-\varphi)\mathbb{I} + \varphi[\mathbb{I} - \mathbb{P}_{cyl} : \mathbb{C}]^{-1}]^{-1}, \quad (39)$$

where $\mathbb{I}, I_{ijkl} = (\delta_{ik}\delta_{jl} + \delta_{il}\delta_{jk})$, is the fourth-order unity tensor, and where $\mathbb{P}_{cyl}$ is a fourth-order (symmetric) tensor depending on the shape of cylindrical inclusions and on the stiffness tensor $\mathbb{C}$ of the (herein isotropic) matrix (components see Table 7, column two). The non-zero tensor components of $\mathbb{P}_{cyl}$ read as (see e.g. [34])

$$P_{1111} = P_{2222} = P(5C_{1111} - 3C_{1122}), \quad P_{1122} = -P(C_{1111} + C_{1122}),$$
$$P_{1313} = P_{2323} = 2PC_{1111}, \quad \text{and} \quad P_{1212} = P(3C_{1111} - C_{1122}), \quad (40)$$

with $P = 1/(8C_{1111}(C_{1111} - C_{1122}))$.

A.4. Unit cell method for effective elastic properties of a solid matrix perforated by hexagonally arranged, parallel cylindrical pores

The unit cell is subjected to periodic (symmetric or antisymmetric) boundary conditions for the displacements [9], such that the spatial averages of the corresponding strains are equal to the macroscopic strains related to the porous material. Linking these macroscopic strains to the spatial average of the periodic microstresses they provoke, i.e. to the macroscopic stresses, yields the homogenized effective stiffness of the porous material. In detail, four independent displacement configurations are imposed on the boundary of the unit cell to provoke unit values of macroscopic strain components. More specifically, the spatial averages of the corresponding periodic (normal and shear) microstresses are equal to the components of the homogenized stiffness tensor of the porous material.

Four finite element models of unit cells (consisting of 6550, 8690, 13,104, and 19,750 eight-node linear brick elements,

respectively) were built in ABAQUS according to Fig. 1c (see Table 6 and Eq. (19) for pore-diameter-over-pore-distance ratios *d/e* related to different porosities), in order to represent the microstructure of the specimens making up *set C*. No significant changes in elastic stiffnesses were observed when (almost 200,000) elements half the size of the aforementioned elements were used for representation of specimen *C-4*, so that the numerical results indicated by circles and squares in Figs. 12 and 13 can be considered as converged in the sense of a sufficiently fine finite element discretization [93].

References

[1] Arenberg D. Ultrasonic solid delay lines. J Acoust Soc Am 1948;20(1):1–26.
[2] Ashman R, Cowin S, Van Buskirk W, Rice J. A continuous wave technique for the measurement of the elastic properties of cortical bone. J Biomech 1984;17(5):349–61.
[3] Auld B. Acoustic fields and waves in solids, vol. I. 2nd ed. Canada: John Wiley & Sons Toronto; 1990.
[4] Authier A, Zarembowitch A. International tables for crystallography. International union of crystallography. Experimental determination of elastic constants, vol. D; 2006. p. 88–9 [Chapter 1.3.4.6].
[5] Barenblatt G. Scaling, self-similarity, and intermediate asymptotics. 1st ed.. Cambridge (England): Cambridge University Press; 1996.
[6] Benck R, Filbey G. Elastic constants of aluminum alloys 2024-T3510, 5083-H131, and 7039-T64 as measured by a sonic technique. Memorandum report no. 2649, USA Ballistic Research Laboratories; 1976.
[7] Benveniste Y. A new approach to the application of Mori-Tanaka's theory in composite materials. Mech Mater 1987;6:147–57.
[8] Berryman J. Long-wavelength propagation in composite elastic media I.Spherical inclusions. J Acoust Soc Am 1980;68(6):1809–19.
[9] Böhm H. A short introduction to continuum micromechanics. In: Böhm H, editor. Mechanics of microstructured material. CISM lecture notes no. 464. Wien – New York: Springer; 2004. p. 1–40.
[10] Bose S, Mal A. Longitudinal shear waves in a fiber-reinforced composite. Int J Solids Struct 1973;9:1075–85.
[11] Bose S, Mal A. Elastic waves in a fiber-reinforced composite. J Mech Phys Solids 1974;22:217–29.
[12] Buckingham E. On physically similar systems. Illustrations of the use of dimensional analysis. Phys Rev 1914;4(4):345–76.
[13] Bucur V, Archer R. Elastic constants for wood by an ultrasonic method. Wood Sci Technol 1984;18:255–65.
[14] Carcione J. Wave fields in real media: wave propagation in anisotropic, anelastic and porous media, handbook of geophysical exploration – seismic exploration, 1st ed., vol. 31. Oxford (United Kingdom): Pergamon, Elsevier Science Ltd.; 2001.
[15] Chree C. The equations of an isotropic elastic solid in polar and cylindrical coordinates, their solutions and applications. Trans Cambridge Philos Soc Math Phys Sci 1889;14:250–369.
[16] Christoffel E. Über die Fortpflanzung von Stößen durch elastische feste Körper. Ann Math Pura Appl 1877;8(II):193–243 [in German].
[17] Christoffel E. Untersuchungen über die mit dem Fortbestehen linearer partieller Differentialgleichungen verträglichen Unstetigkeiten. Ann Math Pura Appl 1877;8(II):81–112 [in German].
[18] Datta S. Self-consistent approach to multiple scattering by elastic ellipsoidal inclusions. Am Soc Mech Engrs 1977;77:657–62.
[19] Dean G, Turner P. The elastic properties of carbon fibers and their composites. Composites 1973;4(4):174–80.
[20] Drugan W, Willis J. A micromechanics-based nonlocal constitutive equation and estimates of representative volume element size for elastic composites. J Mech Phys Solids 1996;44(4):497–524.
[21] EN-485-1, 2007. Aluminium and aluminum alloys – sheets, strip and plate – Part 1: Technical conditions for inspection and delivery. German version.
[22] EN-485-2, 2006. Aluminium and aluminum alloys – sheets, strip and plate – Part 2: Mechanical properties. German version.
[23] Eshelby J. The determination of the elastic field of an ellipsoidal inclusion, and related problems. Proc Phys Soc London 1957;A241:376–96.
[24] Fedorov F. Theory of elastic waves in crystals. New York (USA): Plenum Press; 1968.
[25] Firestone F, Frederick J. Refinements in supersonic reflectoscopy. Polarized sound. J Acoust Soc Am 1946;18(1):200–11.
[26] Foldy L. The multiple scattering of waves. J Theor Biol 1945;67(3):107–19.
[27] Gubernatis J, Domany E. Effects of microstructure on the speed and attenuation of elastic waves in porous materials. Wave Motion 1984;6:579–89.
[28] Hartmann B, Jarzynski J. Immersion apparatus for ultrasonic measurements in polymers. J Acoust Soc Am 1974;56(5):1469–77.
[29] Hashin Z, Rosen B. The elastic moduli of fibre-reinforced media. J Appl Mech 1964;31:223–32.
[30] Hayashi T, Song W, Rose J. Guided wave dispersion curves for a bar with an arbitrary cross-section, a rod and rail example. Ultrasonics 2003;41:175–83.
[31] Hayashi T, Tamayama C, Murase M. Wave structure analysis of guided waves in a bar with an arbitrary cross-section. Ultrasonics 2006;44:17–24.
[32] Hearmon R. The elastic constants of anisotropic materials. Rev Mod Phys 1946;18(3):409–40.
[33] Helbig K. Foundations of anisotropy for exploration seismics. Handbook of geophysical exploration, 1st ed., vol. 22. Oxford (England): Pergamon Press; 1994.
[34] Hellmich C, Barthelemy J, Dormieux L. Mineral–collagen interactions in elasticity of bone ultrastructure – a continuum micromechanics approach. Eur J Mech A/Solids 2004;23:783–810.
[35] Hlavacek M. A continuum theory for fibre-reinforced composites. Int J Solids Struct 1975;11:199–211.
[36] Hueter T. Ultrasonic velocity dispersion in solid rods. J Acoust Soc Am 1950;22:514–5.
[37] Huntington H. Ultrasonic measurements on single crystals. Phys Rev 1947;72(4):321–31.
[38] Huntington H. On ultrasonic scattering by polycrystals. J Acoust Soc Am 1950;22(3):362–4.
[39] Ivey D, Mrowca B, Guth E. J Appl Phys 1949;20:486–92.
[40] Karki B, Stixrude L, Wentzcovitch R. High-pressure elastic properties of major materials of earth's mantle from first principles. Rev Geophys 2001;39(4):507–34.
[41] Kino G. Acoustic waves: devices, imaging, and analog processing. New Jersey (USA): Englewood Cliffs; 1987.
[42] Kinra V, Anand A. Wave propagation in a random particulate composite at long and short wavelengths. Int J Solids Struct 1982;18(5):367–80.
[43] Kohlhauser C. Elasticity tensor determination by means of ultrasonic pulse transmission: application ranges in terms of specimen geometry and microstructure, off-diagonal tensor components, as well as different engineering and biomedical materials. Doctoral thesis, Vienna University of Technology, Vienna, Austria; 2009.
[44] Kohlhauser C, Hellmich C. Determination of Poisson's ratios in isotropic, transversely isotropic, and orthotropic materials by means of combined ultrasonic-mechanical testing of normal stiffnesses: application to metals and wood. Eur J Mech A/Solids 2012;33(May):82–98.
[45] Kohlhauser C, Hellmich C, Vitale-Brovarone C, Boccaccini A, Rota A, Eberhardsteiner J. Ultrasonic characterisation of porous biomaterials across different frequencies. Strain 2009;45(1):34–44.
[46] Kolsky H. Stress waves in solids. London (United Kingdom): Oxford University Press; 1953.
[47] Kolsky H. Stress waves in solids. J Sound Vib 1964;1:88–110.
[48] Kriz R, Stinchcomb W. Elastic moduli of transversely isotropic graphite fibers and their composites. Exp Mech 1979;19(2):41–9.
[49] Lax M. Multiple scattering of waves. II. The effective field in dense systems. Phys Rev 1952;85(4):621–9.
[50] Lazarus D. The variation of the adiabatic elastic constants of KCl, NaCl, CuZn, Cu, and Al with pressure to 10,000 bars. Phys Rev 1949;76(4):545–53.
[51] Ledbetter H. Sound velocities and elastic-constant averaging for polycrystalline copper. J Phys D: Appl Phys 1980;13:1879–84.
[52] Ledbetter H, Datta S. Effective wave speeds in an SiC-particle-reinforced Al composite. J Acoust Soc Am 1986;79(2):239–48.
[53] Ledbetter H, Frederick N, Austin M. Elastic-constant variability in stainless-steel 304. J Appl Phys 1980;51(1):305–9.
[54] Li S. General unit cells for micromechanical analyses of unidirectional composites. Composites 2000;A32:815–26.
[55] Love A. A treatise on the mathematical theory of elasticity. 2nd ed. University Press; 1906.
[56] Makarynska D, Gurevich B, Ciz R, Arns C, Knackstedt M. Finite element modelling of the effective elastic properties of partially saturated rocks. Comput Geosci 2008;34:647–57.
[57] Markham M. Measurements of elastic constants by the ultrasonic pulse method. Br J Appl Phys 1957;8(S6):56–63.
[58] Markham M. Correlation between the elastic constants of polycrystalline aggregates and single crystals. Mater Res 1962;1(2):107–14.
[59] Markham M. Measurements of the elastic constants of fibre composites by ultrasonics. Composites 1970;1:145–9.
[60] Mason W, McSkimin H. Energy losses of sound waves in metals due to scattering and diffusion. J Appl Phy 1948;19:940–6.
[61] Matweb. Automations Creations Inc., Material type: aluminum alloy 5083-H112; 2009. <http://www.matweb.com>.
[62] McSkimin H. Propagation of longitudinal waves and shear waves in cylindrical rods at high frequencies. J Acoust Soc Am 1956;28(3):484–94.
[63] Mori T, Tanaka K. Average stress in matrix and average elastic energy of materials with misfitting inclusions. Acta Metall 1973;21(5):571–4.
[64] Müller J. Some second thoughts on error statements. Nucl Instrum Methods 1979;163:241–51.
[65] Murakami H, Maewal A, Hegemier G. Mixture theory for longitudinal wave propagation in unidirectional composites with cylindrical fibers of arbitrary cross section – I. Formulation. Int J Solids Struct 1979;15:325–34.
[66] Murakami H, Maewal A, Hegemier G. Mixture theory for longitudinal wave propagation in unidirectional composites with cylindrical fibers of arbitrary cross section – II. Computational procedure. Int J Solids Struct 1979;15:335–57.
[67] Naimon E, Ledbetter H, Weston W. Low-temperature elastic properties of four wrought and annealed aluminium alloys. J Mater Sci 1975;10(8):1309–16.

[68] Newton I. Philosophiae naturalis principia mathematica. 1st ed. London (United Kingdom): Royal Society; 1687 [in Latin].

[69] Nicholson P, Strelitzki R. On the prediction of Young's modulus in calcaneal cancellous bone by ultrasonic bulk and bar velocity measurements. Clin Rheumatol 1999;18:10–6.

[70] Northwood T. Velocity of dilatational waves in rods. J Acoust Soc Am 1947;19:505.

[71] Papadakis E, Patton T, Tsai Y, Thompson D, Thompson R. The elastic moduli of a thick composite as measured by ultrasonic bulk wave pulse velocity. J Acoust Soc Am 1991;89(6):2753–7.

[72] Parnell W, Abrahams I. Homogenization for wave propagation in periodic fibre-reinforced media with complex microstructure. I. Theory. J Mech Phys Solids 2008;56:2521–40.

[73] Pochhammer L. Über die fortpflanzungsgeschwindigkeiten kleiner Schwingungen in einem unbegrenzten isotropen Kreiszylinder. Z Angew Math 1876;81:325–36.

[74] Rao M, Prasanna Lakshmi K. Shear-wave propagation in rocks and other lossy media: an experimental study. Curr Sci 2003;85(8):1221–5.

[75] Redwood M. Velocity and attenuation of a narrow-band, high-frequency compressional pulse in a solid wave guide. J Acoust Soc Am 1959;31(4):442–8.

[76] Redwood M. Ultrasonic waveguides – a physical approach. Ultrasonics 1963;1(2):99–105.

[77] Rossi G. Measurability. Measurement 2007;40:545–62.

[78] Sabina F, Willis J. A simple self-consistent analysis of wave propagation in particulate composite. Wave Motion 1988;10:127–42.

[79] Salençon J. Handbook of continuum mechanics. Berlin, Heidelberg (Germany): Springer; 2001.

[80] Stanke F, Kino G. A unified theory for elastic wave propagation in polycrystalline materials. J Acoust Soc Am 1984;75(3):665–81.

[81] Suquet P. Elements of homogenization for inelastic solid mechanics. In: Sanchez-Palencia E, Zaoui A, editors. Homogenization techniques for composite media. Lecture notes in physics no. 272. Wien – New York: Springer; 1987. p. 193–278.

[82] Thurston R. Elastic waves in rods and clad rods. J Acoust Soc Am 1978;64(1):1–37.

[83] Tu L, Brennan J, Sauer J. Dispersion of ultrasonic pulse velocity in cylindrical rods. J Acoust Soc Am 1955;27(3):550–5.

[84] Varadan V, Varadan V, Pao Y. Multiple scattering of elastic waves by cylinders of arbitrary cross section.I. SH waves. J Acoust Soc Am 1978;63(5):1310–9.

[85] Waterman P, Truell R. Multiple scattering of waves. J Math Phys 1961;2(4):512–37.

[86] Wei P, Huang Z. Dynamic effective properties of the particle-reinforced composites with the viscoelastic interphase. Int J Solids Struct 2004;41:6993–7007.

[87] Weston W, Naimon E, Ledbetter H. Low temperature elastic properties of aluminum 5083-0 and four ferritic nickel steels. In: Kaufman J, editor. Properties of materials for liquefied natural gas tankage, vol. ASTM STP 579. Boston, MA, USA: American Society for Testing and Materials; May 21–22, 1975. p. 397–420.

[88] Williams J. Ultrasonic wave propagation in cancellous and cortical bone: prediction of some experimental results by Biot's theory. J Acoust Soc Am 1992;91(2):1106–12.

[89] Willis J. A polarization approach to the scattering of elastic waves – II. Multiple scattering from inclusions. J Mech Phys Solids 1980;28:307–27.

[90] Yang R. A dynamic generalized self-consistent model for wave propagation in particulate composites. J Appl Mech 2003;70:575–82.

[91] Yang R, Mal A. Multiple scattering of elastic waves in a fiber-reinforced composite. J Mech Phys Solids 1994;42(12):1945–68.

[92] Zaoui A. Continuum micromechanics: survey. J Eng Mech 2002;128(8):808–16.

[93] Zienkiewicz O, Taylor R. The finite element method. The basis, vol. 1. London (England): Arnold; 2000.